# In-Band Full Duplex Broadband Power Line Communications

Gautham Prasad, Lutz Lampe, and Sudip Shekhar

***Abstract*—In this paper, we introduce in-band full duplexing (IBFD) for broadband power line communication (BB-PLC) systems. Inspired by the use of IBFD in digital subscriber lines, Ethernet, cable communication and recently in wireless communication, we investigate the constraints and requirements for a successful IBFD implementation in BB-PLC. We propose a two-stage IBFD structure consisting of an initial analog isolation using an active hybrid circuit, and a simplified mixed-domain digital echo cancellation procedure to suppress the self interference. Further, we enhance the digital cancellation filter to better adapt to linear periodically time-varying channel conditions, commonly encountered in PLC scenarios. We evaluate our solution under diverse power line channel and noise conditions to examine the overall data rate gains that can be achieved. Lastly, we extend IBFD to multiple-input multiple-output BB-PLC systems that enable faster and/or more robust data transmission.**

***Index Terms*—Full duplex, Broadband power line communication (BB-PLC), Echo cancellation, Linear periodically time-varying (LPTV) channels, Multiple-input multiple-output (MIMO) PLC**

## I. Introduction and Background

BROADBAND power line communication (BB-PLC) is an established technology with application mainly for in-home multimedia and smart grid communication [2]–[4]. Due to the often harsh PLC channel conditions and the power and bandwidth limitations associated with electromagnetic compatibility (EMC) restrictions, improving data rate in BB-PLC networks is a challenging task. For example, the relatively recent HomePlug AV2 standard expanded the signal band up to frequencies of 86 MHz, but EMC restrictions demand a tighter power spectral density mask at above 30 MHz [5]. Another avenue to improve rate is by increasing spectral efficiency. For a given channel quality, this could be accomplished by in-band full duplex (IBFD) communication that simultaneously transmits and receives data on the same power line and in the same frequency band. In addition to potentially doubling the data throughput, IBFD also solves several prevalent networking problems. It provides a physical layer solution to the hidden node problem without the request-to-send and clear-to-send (RTS-CTS) message exchange, and it enables full-duplex relaying, thereby increasing the overall relaying capacity of a multi-hop network [6]. IBFD also assists cognitive PLC systems, which are found to increase data rates significantly in the FM band [7], by allowing simultaneous functioning of spectrum sensing as well as data transmission.

A major hurdle in achieving IBFD is the inherent interference of the transmitted signal with the received signal-of-interest (SOI). Although the transceiver has knowledge of its own transmitted signal, it cannot directly subtract it from the received signal, since it passes through various analog components before interfering with the SOI. Hence, this self-interference channel needs to be estimated in order to reconstruct and cancel the effective self-interfering signal. Cancellation of this transmitted signal component from the received signal is a form of echo cancellation (EC), which has long been used in telephone networks [8], [9], digital subscriber line (DSL) and cable modems [10]–[17], and Ethernet applications [18], [19]. More recently, IBFD has also been applied to wireless communication systems, e.g., [20]–[24].

### A. IBFD State-of-the-art in PLC

The use of digital EC for PLC is also not new. It has traditionally been used in narrowband (NB) PLC systems to improve spectral efficiency in the small transmission bandwidth available. The IEC 62488 standard [25], which specifies PLC for power utility applications, includes an optional use of EC to improve bandwidth utilization in full-duplex operation. Implementation of echo cancelers for such systems is relatively uncomplicated, typically making use of an adaptive filter tuned using, for example, the least mean squares (LMS) algorithm, to emulate the echo channel. Advancements to such LMS-driven filters have recently been proposed in [26], [27], which have suggested effective methods to reset the filter weights under abrupt channel changes. However, these techniques cannot directly be used for BB-PLC systems. For example, EC for NB-PLC addressed in [26], [27] consider a sampling rate of 25.6 kHz, and hence a bandwidth of less than 15 kHz. BB-PLC systems typically work with a sampling rate of 75 MHz over a bandwidth of 28 MHz [28]. This results in much longer responses of the self-interference channel, and it is thus preferable not to do EC in time domain as in [25]–[27]. Furthermore, channel attenuation varies widely in the transmission band of BB-PLC. For example, [26] considered a constant channel attenuation of about 32 dB for NB-PLC. But for realistic BB-PLC channels, we consider channel attenuations between 10 dB and 80 dB in the frequency band of interest. This makes EC challenging since, as we will show, low attenuation impedes adaptation of the EC filter while high attenuation

The authors are with the Department of Electrical and Computer Engineering, The University of British Columbia. Email: {gauthamp, lampe, sudip}@ece.ubc.ca.

Early ideas and initial results of this work were presented at the 9th Workshop on Power Line Communications, Klagenfurt, Austria, September 2015. A part of this work was also presented at the IEEE International Symposium on Power Line Communication and its Applications (ISPLC), Bottrop, Germany, March 2016 [1].

This work was supported by the Natural Sciences and Engineering Research Council of Canada (NSERC).

leads to high quantization noise from self interference. Finally, the PLC network impedance varies widely in the BB-PLC spectrum, which, compared to NB-PLC, complicates signal isolation through the analog front-end.

### B. Outline and Contributions

Against the background of existing IBFD schemes for different media and systems, in this paper, we present the first design for IBFD enabled BB-PLC transceivers. We start in Section II with an analysis for the cancellation gain required, the dynamic range of typical Analog-to-Digital Converters (ADCs), and the level of non-linear signal components in a BB-PLC scenario. This analysis guides us to propose a two-step cancellation scheme in Section III. This cancellation scheme uses a hybrid module in the analog domain, and a subsequent time/frequency domain adaptive cancellation scheme for self-interference suppression in the digital domain. Our design takes the effect of unknown and varying network impedances into account and facilitates simultaneous operation of a low impedance transmitter path and a high impedance receiver path that is commonly the case in BB-PLC modems [3, Ch. 4.2.7]. To address linear periodically time varying (LPTV) channel conditions that are often observed in power line channels [29], in Section IV, we propose a new LPTV-aware LMS algorithm that provides more accurate echo estimates by exploiting the cyclic nature of short-term channel variations. We demonstrate the benefits of our IBFD design in Section V, by showing the results of a simulative performance study as well as theoretical data rate gain calculations obtained under different channel and noise conditions focusing on in-home PLC network scenarios. We then extend our solution to a multiple-input multiple-output (MIMO) system and provide its performance analysis in Section VI. Finally, conclusions are offered in Section VII.

## II. Feasibility and Requirements of IBFD for BB-PLC

The amount of cancellation required for a successful IBFD functioning depends on the SOI strength, as well as the noise floor at the receiver ($N_{\mathrm{R}}$). To completely erase the effects of self interference (SI), ideally, the power spectral density (PSD) of the residual SI (RSI), $P_{\mathrm{RSI}}$, should be less than $N_{\mathrm{R}}$. In such a case, data rates can be successfully doubled through IBFD.

Admissible transmit PSDs of BB-PLC standards vary mainly as a function of frequency band and geographical region, so as to meet the applicable EMC regulations [3, Chs. 3, 9], [4, Ch. 6.4]. We adopt a maximum PSD of $P_{\mathrm{TX}} = -50$ dBm/Hz, which is specified in the HomePlug AV (HPAV) standard for North America [28] and corresponds to a worst-case analysis for IBFD, as it produces the largest gap between SI and noise floor and thus requires the greatest cancellation gain. The value of $N_{\mathrm{R}}$ varies significantly based on frequency band, network conditions such as number of loads connected to the line, types of loads, types of interconnections and the overall network topology. Typical values of $N_{\mathrm{R}}$ for in-home PLC environments are greater than $-130$ dBm/Hz [30]–[33]. This produces a maximum cancellation gain requirement of less than $-50-(-130) = 80$ dB.

Next, we consider the possibility of ADC saturation due to relatively high SI in the analog domain. Typical BB-PLC receivers use a 12-bit ADC, which gives an ideal signal-to-quantization-noise ratio (SQNR) of 74 dB. However, commercial 12-bit ADCs, such as AD9866[1], provide a typical Signal-to-Noise-and-Distortion-Ratio (SINAD) of 69 dB. This is further reduced considering the application of multi-carrier transmission and in particular orthogonal-frequency division multiplexing (OFDM) as used in BB-PLC. For an $n$-bit ADC with an effective number of bits of ENOB, we have [34, Ch. 6]

$$\mathrm{SINAD} = \frac{\sigma_x^2}{\sigma_e^2} = \frac{12(2^{\mathrm{ENOB}-1})^2}{\mathrm{PAPR}} \tag{1}$$

and thus,

$$\mathrm{SINAD}_{\mathrm{dB}} = 6.02\mathrm{ENOB} - \mathrm{PAPR}_{\mathrm{dB}} + 4.77 \text{ dB} , \tag{2}$$

where $\mathrm{PAPR}_{\mathrm{dB}}$ is the peak-to-average-power ratio of the input signal in dB, and $\sigma_x^2$ and $\sigma_e^2$ are the variances of the input signal and the uniformly distributed quantization error, respectively. For OFDM transmission, the value of PAPR depends on the number of sub-carriers used for data transmission. For example, although the HPAV specification uses a 3072-point discrete Fourier transform (DFT), only $N_{\mathrm{used}} = 917$ of those sub-carriers are used for data transmission in the $2-28$ MHz bandwidth [28]. Such systems can have a maximum PAPR of $10\log_{10}(917) = 29.67$ dB, which would significantly decrease the SINAD in (2). However, to reduce the PAPR in such scenarios, signals beyond a certain maximum amplitude $V_{\mathrm{clip}}$ are clipped, resulting in additional clipping noise that decreases with increasing $V_{\mathrm{clip}}$. But setting a large $V_{\mathrm{clip}}$ incurs substantial quantization noise [35], [36]. We therefore need to choose an optimized clipping amplitude $V_{\mathrm{clip}}^{\mathrm{opt}}$, and it has been shown that $V_{\mathrm{clip}}^{\mathrm{opt}} = 5\sigma_x$ is a good choice for a 12-bit ADC [36]. With this $V_{\mathrm{clip}}^{\mathrm{opt}}$, our simulation results indicate a SINAD of 60 dB for a 12-bit ADC, closely matching the theoretical values in [36]. As a consequence, the IBFD system contains a quantization noise level of at most $P_{\mathrm{QN}} = -50-60 = -110$ dBm/Hz. Note that, in reality, $P_{\mathrm{QN}} < -110$ dBm/Hz, depending on the amount of analog signal suppression experienced by the SI before reaching the ADC. Hence, the quantization noise becomes comparable to the noise floor in typical PLC scenarios.

High SI also generates non-linear signal components in the analog front-end (AFE), which then introduce additional interference with the SOI. Such interferences are mitigated in Ethernet and wireless systems by analog cancellation circuits [18], [19], [21]. However for BB-PLC, efficient AFEs [37] hold total non-linear distortion levels at 75 dB to 80 dB below the transmit power. With a $P_{\mathrm{TX}}$ of $-50$ dBm/Hz, the non-linear distortion levels are less than $-50-75 = -125$ dBm/Hz, which are lower than typical $N_{\mathrm{R}}$ values and less than $P_{\mathrm{QN}}$, and hence have negligible effect on SOI.

[1] AD9866 is manufactured specifically for power line networking and works up to 80 Msps that suits the 75 MHz HPAV applications.

The above analysis shows that the isolation required is significant, but notably less than what is needed in wireless IBFD (about 110 dB or more). This suggests that we may not need a three-step cancellation approach consisting of analog isolation through a hybrid, analog circuit-based cancellation (ACC), and digital EC as often considered in wireless communications [20], [21], [23]. Toward a simpler design, we suggest to omit the ACC component, as digital EC has the advantages of better reconfigurability and adaptivity. These features are essential for IBFD in BB-PLC where the interference-channel conditions can vary widely over installation, and over time for a given installation, due to the widely varying network impedance. Furthermore, ACC schemes based on delay-line solutions presented in e.g. [20] would be difficult to adopt for BB-PLC due to the length of expected delays. On the other hand, digital EC schemes considered for DSL systems (e.g. [10], [14], [15], [17]) seem to be an excellent starting point for digital EC in BB-PLC.

## III. Proposed Two-step Cancellation Procedure for IBFD Implementation

Following the discussion in the previous section, we propose the two-step cancellation procedure consisting of

(a) an analog domain isolation using a hybrid
(b) a digital domain echo cancellation.

### A. Analog Isolation

IBFD techniques in wireless communications use a ferrite circulator to gain up to 15 dB of analog isolation between the transmitted signal and the SOI [20]. Due to cost and size limitations of ferrite circulators, a simpler transformer-based hybrid was also developed for such applications [38]. But the size of the magnets and transformers in ferrite circulators and transformer hybrids, respectively, prohibits their use in low frequency applications (say, for $< 100$ MHz) such as BB-PLC. We therefore choose an active hybrid circuit as in [39], and similar to the ones used in DSL operations [12], [40]. This circuit uses three amplifier and voltage divider stages to provide complete voltage transfer from one port to its adjacent port in one direction, and utilizes the high reverse isolation of operational amplifiers (op-amps) to provide isolation in the opposite direction.

The location of the hybrid in the overall IBFD system can be seen from Fig. 3 (which is discussed in detail in Section III-B), where the port 1 (P1) of the hybrid is connected to the transmitter-end AFE, port 2 (P2) to the power line channel, and port 3 (P3) to the receiver-end AFE of the transceiver. For our application, since the hybrid has only two inputs, at P1 from the transmitter and at P2 from the channel, we simplify the existing circuit from [39] by abandoning the amplifier stage at P3, as there is no voltage transfer required from P3 to P1. Fig. 1 shows the circuit schematic of the simplified active hybrid using the Advanced Design System (ADS) software. This simplification reduces the power consumption of the hybrid by over 30%, without compromising its operation for the use case considered here.

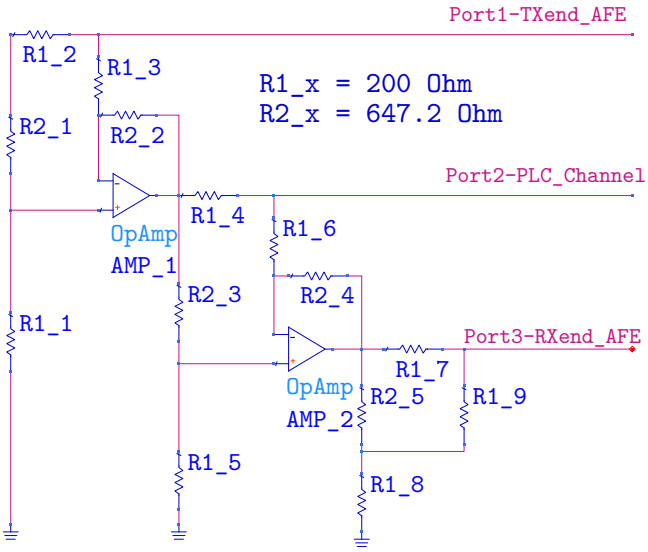


Fig. 1. ADS schematic of the simplified hybrid implementation with only two op-amps, and the resistances tuned to provide port impedances of $Z_1 = Z_2 = Z_3 = 100\ \Omega$.

The hybrid circuit also gives us the flexibility to set the impedance at each port, $Z_i$, individually, where $i \in \{1, 2, 3\}$ indicates the port number. The hybrid circuit in Fig. 1 operates in such a way that when a voltage is applied at port $i$, it is transferred out of port $i + 1$ across a matched load, for $i = 1, 2$. Therefore, we would ideally want to match P2 and P3 to the power line channel and receiver-end AFE, respectively. Additionally, impedance matching at P2 also prevents reflections from the hybrid-to-channel interface that are then transferred to the receiver at P3 causing SI. But impedance matching at P2 is not an easy exercise since the power line channel impedance is unknown and varies with both time and frequency. Adaptive impedance matching circuits (e.g. [41]) are not able to achieve matching over the entire operating frequency range of BB-PLC. We therefore set $Z_2 = 100\ \Omega$, which is the typical impedance of a power line channel in our frequency range of interest, cf. e.g. [4, Ch. 1]. Similarly, we match the impedance $Z_3 = Z_{\mathrm{RX}}$ at P3. Although the receiver-end AFE usually presents a high impedance [42], it is typically preceded by an impedance matching section which attempts to match the receiver-end input impedance to the line impedance of about $100\ \Omega$ [42]. Hence, it makes sense to set $Z_3 = 100\ \Omega$. On the other hand, at P1, we desire to bridge the impedance to obtain maximum voltage transfer and draw minimum current. We achieve this by having $Z_1 \gg Z_{\mathrm{s}}$, where $Z_{\mathrm{s}}$ is the output impedance of the transmitter-end AFE. Typically, the value of $Z_{\mathrm{s}}$ is very low, e.g., of the order of $3\ \Omega$ [42]. Hence, $Z_1 = 100\ \Omega$ suffices to achieve impedance bridging.[2] Therefore, we tune the resistances in our hybrid circuit to set $Z_i = 100\ \Omega$, $i = 1, 2, 3$, which is shown in Fig. 1. This can easily be achieved by doubling all the resistances from the original circuit of [39], which presents an impedance of $50\ \Omega$ at all ports. Doubling all the impedances also ensures

[2]Alternatively, we could match the impedances at P1 by setting $Z_1 = Z_{\mathrm{s}}$, but this would halve the voltage transfer into the channel, and line drivers typically cannot drive such low impedances (e.g., less than $10\ \Omega$ [42]).

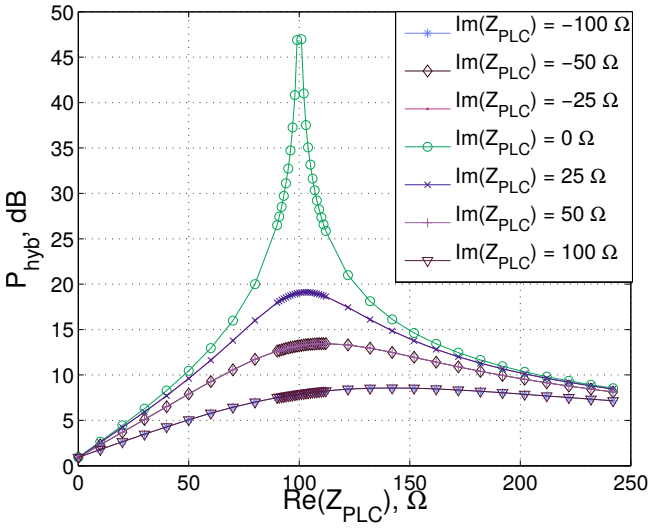


Fig. 2. Hybrid isolation $P_{\rm hyb}$ from port 1 to port 3 as a function of PLC line impedance $Z_{\rm PLC}$. $P_{\rm hyb}$ is maximum when the line impedance is matched to the hybrid P2 impedance, i.e., $Z_{\rm PLC} = Z_2 = (100 + j0)\ \Omega$.

appropriate functioning of the voltage divider sections.

From the above it follows that the hybrid circuit has a two-fold purpose in IBFD for BB-PLC. It provides well defined impedances for the transmitter and receiver chains of the AFE and it isolates them from each other. While, due to the hybrid, there is no direct SI path from the transmitter to the receiver, the isolation is imperfect because of reflections at P2. More specifically, with a channel impedance $Z_{\rm PLC}(f)$ for some frequency $f$, we have the reflection coefficient

$$\Gamma_{\rm PLC}(f) = \frac{Z_{\rm PLC}(f) - Z_2(f)}{Z_{\rm PLC}(f) + Z_2(f)}\ , \tag{3}$$

where $Z_2(f) = Z_2 = 100\ \Omega$. For the hybrid shown in Fig. 1, we obtain the voltage transfer function from P1 to P3 as $H_{\rm SI}(f) = 0.9\ \Gamma_{\rm PLC}(f)$. The derivation is relegated to Appendix B-A. The resulting hybrid isolation $P_{\rm hyb} = -20\ \log_{10}|H_{\rm SI}|$ is shown as a function of $Z_{\rm PLC}$ in Fig. 2. We observe an isolation of about 45 dB when P2 is nearly matched. But as $Z_{\rm PLC}$ deviates from the matched value of $Z_2 = 100\ \Omega$, the isolation $P_{\rm hyb}$ drops quickly. $P_{\rm hyb}$ also depends on the bandwidth of the op-amps used in Fig. 1, where op-amps with a larger bandwidth provide a more constant hybrid isolation across frequencies. Considering the cost and availability we apply op-amps with a 300 MHz operating bandwidth.

Since $P_{\rm hyb}$ is insufficient to improve the signal-to-interference-plus-Noise (SINR) of the received signal to a sufficient level under the commonly encountered mismatched-port scenario, the remaining cancellation is performed by an echo canceler in the digital domain.

### B. Digital Echo Cancellation

Since all recently standardized BB-PLC systems apply multi-carrier transmission and most of them in the form of OFDM, it is meaningful to consider implementations of digital EC in time and frequency domain as well as their combination. For this we make use of designs presented in previous work in the context of DSL [10], [14], [15], [17]. Fig. 3 shows the block diagrams for the corresponding IBFD solutions, including the connection of digital EC and the hybrid circuit discussed in the previous section. In the following, we briefly review the different digital EC schemes and discuss and compare their applicability for IBFD in BB-PLC.

*1) Time-Domain Cancellation:* The time-domain based cancellation is shown in the right part of Fig. 3(a). The time-domain transmit signal $x$ is tapped just before it enters the AFE and is used together with the time-domain received signal $y$ to tune the weights $\boldsymbol{g} = [g_1, \ldots, g_M]^{\rm T}$ of an adaptive filter to learn the effective echo channel $h_{\rm SI}$ from P1 to P3.

To derive the filter update, we express the received signal sample at discrete time $n$ as ('$*$' indicates linear convolution)

$$y(n) = \underbrace{(x * h_{\rm SI})(n)}_{\text{echo}} + \underbrace{(x_{\rm SOI} * h_{\rm PLC})(n)}_{\text{SOI}} + \underbrace{w(n)}_{\text{cumulative noise}}\ , \tag{4}$$

where $x_{\rm SOI}$ is the far-end transmitted signal which passes through the PLC channel with impulse response $h_{\rm PLC}$, and $w(n)$ represents the noise at the receiver end. The echo estimate $\hat{y}(n)$ produced by the filter $\boldsymbol{g}$ is given by

$$\hat{y}(n) = \boldsymbol{x}^{\rm T}(n)\boldsymbol{g}(n)\ , \tag{5}$$

where $\boldsymbol{x}(n) = [x(n-M+1)\ldots x(n)]^{\rm T}$. As a low-complexity solution for tuning the filter weights, we apply the LMS update

$$\boldsymbol{g}(n+1) = \boldsymbol{g}(n) + \mu\boldsymbol{x}(n)e(n)\ , \tag{6}$$

where

$$e(n) = y(n) - \hat{y}(n) \tag{7}$$

and $\mu > 0$ is the step size of the LMS adaptation. We note that baseband transmission is applied for BB-PLC and thus no complex-conjugate operator is required in (6).

The number of weights $M$ in the adaptive filter is decided based on the actual length of typical echo channels. Fig. 4 shows the frequency responses for four sample PLC channels (Fig. 4(a)) and their corresponding SI channels (Fig. 4(b)) considering different in-home PLC network conditions. The channels are generated using the procedure described in Appendix A-A. Considering a sampling frequency of $f_{\rm s} = 75$ MHz and a 3072-point DFT as applied in HPAV [28], Fig. 4(c) shows the corresponding impulse response of the echo channel $h_{\rm SI}$. We observe that about $M = 40$ would be a reasonable filter length to fully capture the effect of echoes.

*2) Frequency-Domain Cancellation:* EC can also be implemented in the frequency domain, which typically reduces the computational complexity associated with the estimation step (5). The frequency-domain EC for BB-PLC is shown in the left part of Fig. 3(a). Let us define the $\ell$th frequency-domain transmit vector (i.e., OFDM symbol) $\boldsymbol{X}(\ell) = [X_1(\ell), \ldots, X_{N_{\rm used}}(\ell)]^T$, and the corresponding received and error vector $\boldsymbol{Y}(\ell)$ and $\boldsymbol{E}(\ell)$, respectively. The number of elements in the adaptive filter vector $\boldsymbol{G}$ is equal to the number of used OFDM sub-carriers, i.e., $M = N_{\rm used}$. The echo estimate in the frequency domain is then obtained as ('$\cdot$' denotes element-wise multiplication)

$$\hat{\boldsymbol{Y}}(\ell) = \boldsymbol{X}(\ell) \cdot \boldsymbol{G}(\ell)\ , \tag{8}$$

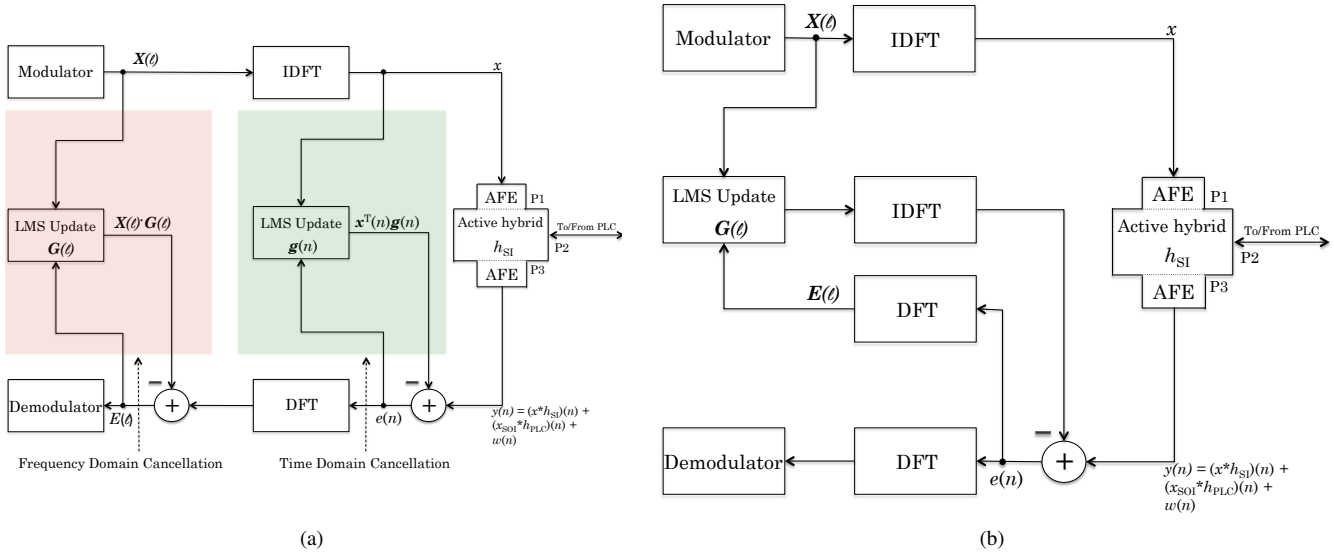


Fig. 3. Transceiver block diagram for IBFD for BB-PLC using OFDM. (a) EC in time and frequency domain (only one of the shaded blocks is used). (b) Mixed-domain EC. For brevity, we include addition and removal of cyclic prefix with the IDFT and DFT blocks, respectively.

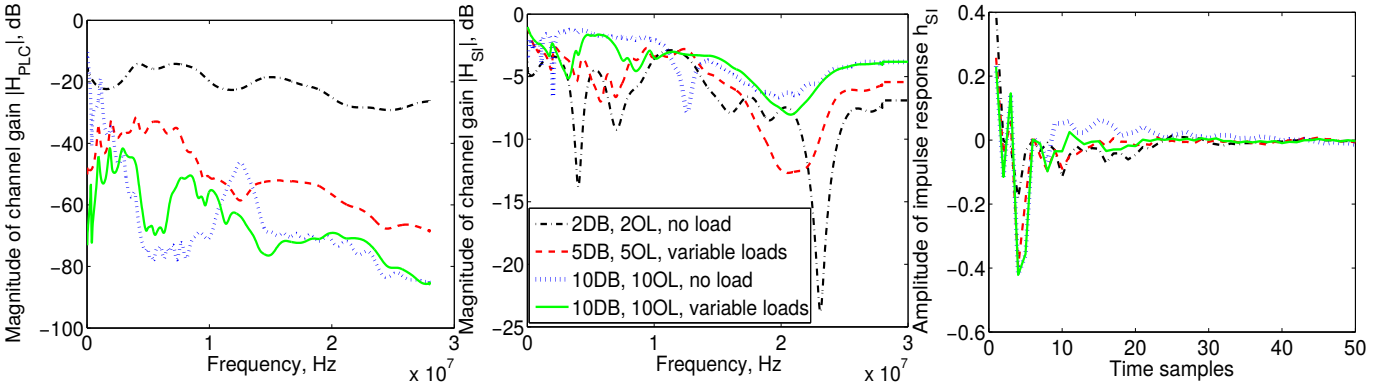


Fig. 4. Magnitude of channel gain of (a) sample PLC channels under different in-home network conditions, and the (b) frequency and (c) impulse responses of their corresponding SI/echo channels.

with the LMS filter update

$$\boldsymbol{G}(\ell+1) = \boldsymbol{G}(\ell) + \mu \mathrm{diag}(\boldsymbol{X}(\ell))^* \boldsymbol{E}(\ell) \;, \tag{9}$$

where $\mathrm{diag}(\boldsymbol{X})$ is the diagonal matrix with the elements of $\boldsymbol{X}$ on the principal diagonal, and the error signal in the frequency domain follows from

$$\boldsymbol{E}(\ell) = \boldsymbol{Y}(\ell) - \hat{\boldsymbol{Y}}(\ell) \;. \tag{10}$$

We notice from Eqs. (8)-(10) and the block diagram in Fig. 3(a) that a successful frequency-domain cancellation with this setup requires synchronous transmission and reception with respect to the OFDM-symbol timing of the transmitted signal and the SOI. To accommodate a frame-asynchronous operation, we move to a simplified mixed-domain EC.

*3) Mixed-Domain Cancellation:* Mixed-domain cancellation captures favorable aspects from both its time- and frequency-domain counterparts, by employing frequency-domain estimation as in (8) for a reduced number of computations, and time-domain cancellation as in (7) for efficient asynchronous cancellation. The corresponding implementation is shown in Fig. 3(b). This type of simplified mixed-domain cancellation is made possible by the fact that BB-PLC systems such as HPAV [28] use a cyclic prefix that essentially eliminates interference between successive OFDM symbols, which avoids the need for the traditional cyclic echo synthesis performed in mixed-domain cancellation in DSL systems [10], [14], [17]. As shown in Fig. 3(b), mixed-domain EC requires two additional DFT/IDFT blocks for time/frequency-domain transformation.

The number of computations required in a time-domain echo canceler (TDEC) depends on $M$. Since the signals and filter taps are real, every LMS iteration requires $2M+1$ real multiplications and $2M$ real additions [43, Ch. 6]. Hence, for every OFDM symbol of size $N$, the total number of real computations required is $(4M+1)N$. In reality, this value is a little higher depending on the length of the cyclic prefix. In the mixed-domain echo canceler (MDEC) on the other hand, the LMS update is performed block-wise, and $M = N_{\mathrm{used}}$. The

TABLE I
NUMBER OF COMPUTATIONS PER OFDM SYMBOL WITH MIXED-DOMAIN AND TIME-DOMAIN ECHO CANCELLATIONS

| | Mixed-domain | Time-domain |
|---|---|---|
| DFT | $4N(2.125p + 4.67q + 6.8r - 3) + 12$ | - |
| Add/Multiply | $22N_{\text{used}}$ | $(4M+1)N$ |
| Total | $4N(2.125p + 4.67q + 6.8r - 3) + 12$ $+22N_{\text{used}}$ | $(4M+1)N$ |

total number of real computations required is approximately $\big(4 \cdot (2 \cdot 1 + 1) + 2 \cdot (2 \cdot 1 + 1) + 2 \cdot (2 \cdot 1)\big)N_{\text{used}} = 22N_{\text{used}}$ [43, Ch. 6]. However, MDEC uses two additional IDFT/DFT blocks. When implemented using a prime factor FFT, where $N = 2^p 3^q 5^r$, these DFT blocks add an approximate overhead of $2N(1.375p + 2.67q + 4r - 1) + 2$ real additions and $2N(0.75p + 2q + 2.8r - 2) + 4$ real multiplications [44]. The overall numbers of computations per OFDM symbol for the TDEC and MDEC schemes are summarized in Table I. For example, for the HPAV specification, using a DFT size of $N = 3072$ and $N_{\text{used}} = 917$ usable carriers, and assuming an echo channel length of 40, TDEC requires 60% more computations than MDEC.

### C. Rate of Convergence and Cancellation Gain

We implement the transceiver designs of Fig. 3(a) for TDEC and Fig. 3(b) for MDEC to compare the rate of convergence (ROC) of the mean-squared error (MSE) using LMS filters. To this end, we adopt the HPAV system specifications for transmission in the $2 - 28$ MHz band and use different in-home channel and noise realizations generated as explained in Appendix A-A and Appendix A-C, respectively.

Fig. 5 shows the MSE for both TDEC and MDEC for one particular power line channel as a function of the time index of the transmitted OFDM symbol, which corresponds to one update in the MDEC implementation. The MSE for MDEC is the average value for all $N_{\text{used}}$ sub-carriers. We also plot the moving average of the fluctuating TDEC MSE that is calculated on a sample-by-sample basis. The small LMS step-size of $\mu = 0.025$ is chosen to better notice the ROC. We observe that the ROC is quite similar for both methods. However, the results indicate a higher EC gain in the steady state for MDEC. This trend has been confirmed in simulation experiments for several PLC channels. Therefore, and because of the computational complexity advantages, we adopt MDEC for our BB-PLC IBFD solution.

Before proceeding, we briefly discuss methods to improve the speed of convergence for MDEC.

*1) Least Squares Initialization:* We can reduce the number of iterations for convergence by replacing a traditional all-zero initialization of $\boldsymbol{G}$ with a least-squares (LS) error estimate [10]. The LS estimate of the echo channel at sub-carrier $k$ can be obtained as

$$\hat{H}_{\text{SI},k} = \frac{Y_k}{X_k} \,. \tag{11}$$

We observed that instead of the all-zero vector initialization, assigning $\boldsymbol{G}(0) = \hat{\boldsymbol{H}}_{\text{SI}}$, where $\hat{\boldsymbol{H}}_{\text{SI}} = [\hat{H}_{\text{SI},1}, \hat{H}_{\text{SI},2}, \ldots, \hat{H}_{\text{SI},k}, \ldots]^{\text{T}}$ for all $k$, increases the ROC significantly, essentially due to a lower MSE starting point.

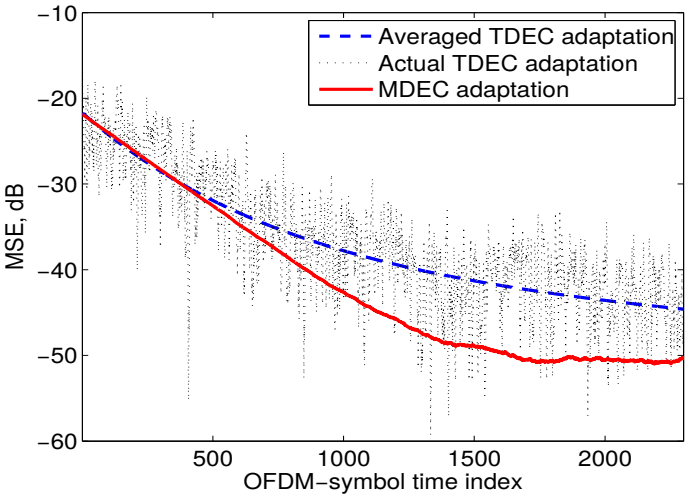


Fig. 5. MSE after EC versus transmitted OFDM-symbol time for a sample PLC channel. Comparison of 40-tap TDEC filter and a 917-tap MDEC. LMS with step-size $\mu = 0.025$.

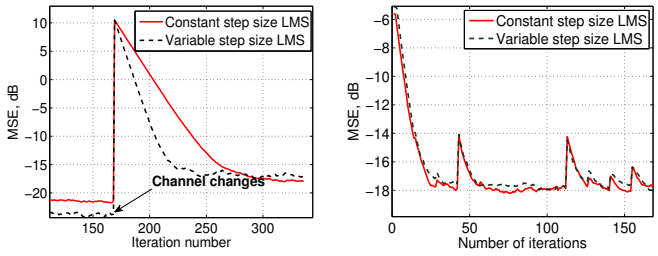


Fig. 6. MSE as a function of MDEC iteration for sample PLC channels generated with [46]. MDEC with fixed and variable step-size LMS. (a) One change of PLC channel. (b) Multiple changes of PLC channel.

*2) Variable Step Size LMS:* To further increase the ROC, we could employ a variable step size LMS (VSS-LMS) algorithm that varies the LMS step size dynamically to provide faster convergence [45]. Fig. 6(a)[3] illustrates this by showing the MSE as a function of the MDEC iteration for the case that the PLC channel changes abruptly due to load changes and thus a new adaptation is required. On the other hand, we observe from Fig. 6(b) that when the channel changes relatively frequently, there is little improvement achieved by using VSS-LMS compared to a constant step size LMS with a larger $\mu$. In Section IV, we present a solution specifically tailored for PLC transmission considering the case that the frequent channel variations have an underlying periodicity.

### D. Implementation of IBFD

The proposed two-stage cancellation structure in Fig. 3(b) requires fairly little changes to the existing modem structure to

[3]Note that the difference in saturated MSE level before the channel change is a result of SNR being conducive for the VSS-LMS to provide a slightly lower MSE with a lower minimum $\mu$ compared to the $\mu$ of the constant step-size LMS. But once the channel changes, both the curves saturate to nearly the same value in the new SNR conditions.

accommodate IBFD. Traditional BB-PLC transceivers are time division duplex devices that use a line-driver control to turn off the transmit or receive path when the other is in operation. Migration of such systems to IBFD is uncomplicated, since it only requires the line driver control to switch on both the transmit and receive paths at the same time to allow simultaneous bidirectional communication. We also note that this ensures complete co-existence and interoperability with the existing half-duplex modems.

The active hybrid circuit also consumes additional power. Our simplified hybrid consists of only two power consuming amplifier sections. With the maximum signal voltage not exceeding 6 V [28], and a typical op-amp supply current of 9 mA [47], the hybrid, on an average, consumes about 108 mW of additional power. Our hybrid port impedance selection also ensures that there is no added power loss in either the transmitted or received signal when compared to a conventional half-duplex system.

## IV. LMS Modification for LPTV PLC channels

The characteristics of PLC channels are determined by the network configuration and topology, the electromagnetic properties of the power lines, and the loads connected at the outlets. Especially the latter are responsible for recurring variations of the PLC channel, as they can be modeled as periodically time-varying impedances in the frequency band of interest for PLC [48]. Such channel changes can cause MSE bursts in the EC performance as illustrated in Fig. 6. Furthermore, the LPTV nature of the changes does not often provide enough time for the LMS algorithm to converge close to its stationary value. In this section, we propose a new LPTV-aware LMS algorithm that specifically exploits the periodic pattern of changes to improve the adaptation.

### A. The LPTV-LMS Adaptation

LPTV loads vary periodically with the period equal to one half of the mains cycle [48]. We therefore divide our LMS adaptation into periods of one half cycle (HC) each. This is also facilitated by typical BB-PLC systems, such as HPAV, which are aware of the mains cycle period [28, Ch. 3]. Denoting $\ell$ as the LMS iteration variable and $\Phi(\ell)$ as the MSE after the $\ell$th iteration, Algorithm 1 shows the pseudo-code of the proposed LPTV-LMS adaptation.

During the "first HC", when $\ell < L_{\mathrm{HC}}$, where $L_{\mathrm{HC}}$ is the number of OFDM symbols in one HC, the MSE is constantly monitored to determine the time locations which experience a cyclic channel change (CCC). Assuming the LMS algorithm does not converge in the first HC[4], the MSE decreases with increasing $\ell$ when there is no change in channel conditions. Therefore, the time at which the MSE increases compared to the previous iteration is identified as the location where a CCC occurs. We record the iteration index $\ell$ of the $j$th such CCC as $c_j$. When a CCC occurs, we have two options: (a) Reset filter weights with an LS estimate, or (b) continue with no reset.

[4]This assumption is valid since the coherence time of LPTV PLC channels [29] is typically much smaller than the LMS convergence time with a legitimate step size.

**Algorithm 1** Pseudo-code for LPTV-LMS algorithm

**First HC:** $\ell = 0, j = 0$
Standard LMS update
**for** $\ell = 1 : L_{\mathrm{HC}} - 1$ **do**
  **if** $\Phi(\ell) - \Phi(\ell-1) > 0$ **then**
    Save $\ell \longrightarrow c_j$  # *Location of a CCC*
    $j = j + 1$
    **if** $\Phi(\ell) - \Phi(\ell-1) \geq \Phi_{\mathrm{reset\_thresh}}$ **then**
      Reset $\boldsymbol{G}(\ell+1)$ with LS estimate
    **else**
      Standard LMS update
    **end if**
  **else**
    Standard LMS update
  **end if**
  $\ell = \ell + 1$
**end for**
**Adaptation HC:** $\ell = 0, j = 0$
**while** 1 **do**  # *Until an N-CCC is encountered*
  **if** $\ell \in \mathscr{C}$ **then**
    $\boldsymbol{G}(\ell) = \boldsymbol{G}(c_{j\oplus 1} - 1)$
    $j = j \oplus 1$
    **if** $\Phi(\ell) - \Phi(c_{j\oplus 1} - 1) > \Phi_{\mathrm{cyclic\_thresh}}$ **then**
      Reset $\boldsymbol{G}(\ell+1)$ with LS estimate
      Jump to First HC
    **end if**
    Standard LMS update
  **else**
    **if** $\Phi(\ell) - \Phi(\ell-1) > \Phi_{\mathrm{change\_thresh}}$ **then**
      Reset $\boldsymbol{G}(\ell+1)$ with LS estimate
      Jump to First HC
    **else**
      Standard LMS update
    **end if**
  **end if**
  $\ell = \ell + 1$
**end while**

If the magnitude of the MSE increase is larger than a preset positive threshold $\Phi_{\mathrm{reset\_thresh}}$, we reset the filter weights with an LS estimate. $\Phi_{\mathrm{reset\_thresh}}$ is chosen based on an average MSE increase caused by an LS estimate reset. This value is obtained from several test runs performed with and without the LS reset. If the MSE increase is less than $\Phi_{\mathrm{reset\_thresh}}$, it indicates that $\Phi(\ell+1)$ with option (a) would be higher than $\Phi(\ell+1)$ with option (b). In such cases, we let the standard LMS adaptation continue without any weight reset. At the end of the first HC, the algorithm contains positions of CCCs in the set $\mathscr{C} = \{c_j |\ j = 0, 1, ..., J-1\}$, where $J$ indicates the total number of CCCs identified in one HC.

After the completion of the first HC, the algorithm jumps to an "adaptation HC", where the values updated in the previous HC are reused to minimize adaptation time. For every $j$th CCC in the current HC, we reset the LMS weights with the last updated value for the corresponding $j$th CCC in the previous HC, i.e., $\boldsymbol{G}(\ell) = \boldsymbol{G}(c_{j\oplus 1} - 1), \forall \ell \in \mathscr{C}$. The symbol '$\oplus$' indicates a modulo $J$ addition to account for cyclic reuse

of weights after $J$ CCCs. This way, we continue the LMS adaption from where we stopped in the previous HC, by reusing the last LMS update of the same channel condition in the previous HC.

We note that the channel conditions undergo non-LPTV changes too. For example, a load connected/disconnected from the line causes a non-CCC (N-CCC). Such changes can occur at positions $\ell \notin \mathscr{C}$ or $\ell \in \mathscr{C}$.

1) To detect N-CCCs at $\ell \notin \mathscr{C}$, we monitor the MSE difference $\Phi(\ell) - \Phi(\ell-1)$ at all $\ell \notin \mathscr{C}$, to check if the value is greater than a threshold $\Phi_{\text{change\_thresh}}$. $\Phi_{\text{change\_thresh}}$ is chosen such that false positives are rarely detected. This is accomplished by setting $\Phi_{\text{change\_thresh}}$ larger than the MSE fluctuations in the steady state of the LMS. Once an N-CCC is detected, we reset the filter weights with an LS estimate and re-start the adaptation by jumping to the "first HC".
2) To detect N-CCCs at $\ell \in \mathscr{C}$, we verify if $\Phi(\ell) - \Phi(c_{j\oplus 1}-1) < \Phi_{\text{cyclic\_thresh}}$. If the condition is not met, we conclude that there has been an N-CCC. We then reset the filter weights with an LS estimate and jump to the "first HC". Generally, $\Phi(\ell) \approx \Phi(c_{j\oplus 1}-1)$, since $\boldsymbol{G}(\ell) = \boldsymbol{G}(c_{j\oplus 1}-1)$. We therefore set a small threshold $\Phi_{\text{cyclic\_thresh}}$ whose value is close to zero.

### B. Performance Illustration

To test MDEC with the proposed LPTV-aware LMS algorithm, we consider in-home channel and noise scenarios as described in Appendix A-A1 and Appendix A-C, respectively.

Fig. 7 shows the MSE as a function of the adaptation iteration against a conventional LMS adaptation. As can be seen in Fig. 7, the CCC locations are determined in the first HC and are subsequently re-used and updated in the following adaption HCs. Notice that for the selected in-home environment, there are two locations in the first HC where the MSE difference crosses the reset threshold limit. These are the locations where the loads displaying commuted behavior switch their impedances and therefore cause a significant change in channel conditions. At these locations, the weights are reset with an LS estimate. For all other CCCs in the first HC, the conventional LMS update is followed. Fig. 7 also clearly demonstrates the superior performance of the LPTV-aware LMS algorithm over the conventional LMS adaption. The re-use of previously updated filter weights results in consistently decreasing MSE over time, which leads to improved SI estimates.

We note that regardless of what LMS algorithm is used, PLC impulse noise, which is known to significantly affect the detection of the SOI, has relatively little effect on the adaptation for SI cancellation, which is due to the relatively large power of the SI signal.

## V. Data Rate Gain Analysis

In this section, we evaluate the gains achievable with the proposed IBFD structure. To this end, we compare the relevant signal-to-noise ratio (SNR) and SINR figures when using half-duplex (HD) and IBFD PLC transmission, respectively. Fig. 8 illustrates the relations of the PSDs at different points

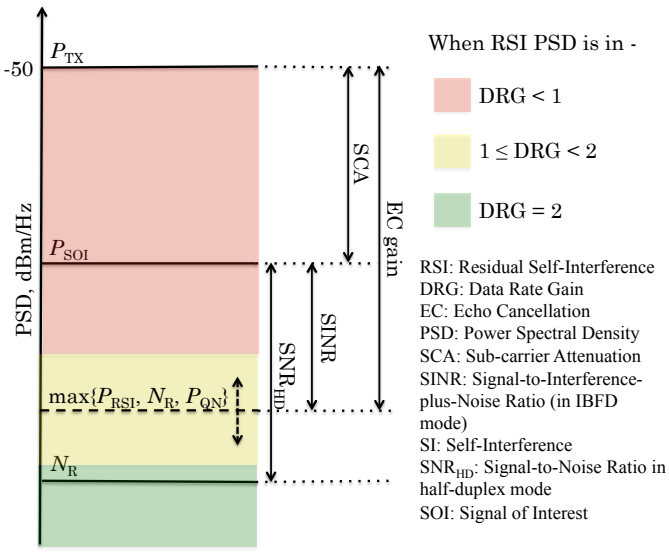


Fig. 8. Per sub-carrier PSD levels at different locations in the PLC transmission system, providing an illustration of achievable data-rate gains (DRGs) using IBFD.

of the transmission system, considering a single sub-carrier associated with a given sub-carrier attenuation (SCA). In HD transmission, the transmit signal with level $P_{\text{TX}}$ is attenuated through the channel, and the SOI is received at the level $P_{\text{SOI}}$. Hence, the per sub-carrier SNR is given by (sub-carriers indices are omitted for brevity)

$$\text{SNR}_{\text{HD}} = P_{\text{SOI}} - N_{\text{R}} \ . \tag{12}$$

In the IBFD case, the transmitted signal is also interference, which after EC by the hybrid and digital adaptive cancellation is experienced at the level $P_{\text{RSI}}$. At the same time, as discussed in Section II, the quantization noise level $P_{\text{QN}}$ may be increased due to the still strong SI signal at the output of the analog hybrid. Hence, the *effective* noise level is equal to

$$P_{\text{eff}} = P_{\text{RSI}} + N_{\text{R}} + P_{\text{QN}} \approx \max\{P_{\text{RSI}}, N_{\text{R}}, P_{\text{QN}}\} \ , \tag{13}$$

where the approximation assumes the domination of one noise or interference component. This yields

$$\text{SINR} = P_{\text{SOI}} - P_{\text{eff}} \tag{14}$$

as the SINR for IBFD.

Comparing SNR for HD and SINR for IBFD leads to the three shaded regions in Fig. 8. As commonly done, we consider the use of adaptive modulation that allocates bits onto sub-carriers to maintain a certain reliability level, commonly expressed through a bit-error rate (BER) target $P_b^{\text{t}}$. Given a modulation with constellation size $M_k$ on a sub-carrier $k$, the BER $P_b$ can be approximated as [49],

$$P_b(\text{SNR}_k, M_k) = \frac{4}{\log_2(M_k)} \cdot \left(1 - \frac{1}{\sqrt{M_k}}\right) \cdot \mathcal{Q}\left(\sqrt{\frac{3 \cdot \text{SNR}_k}{M_k - 1}}\right), \tag{15}$$

where $\text{SNR}_k$ takes the value of $\text{SNR}_{\text{HD},k}$ and $\text{SINR}_k$ for half-duplex and IBFD mode, respectively, and $\mathcal{Q}(x) =$

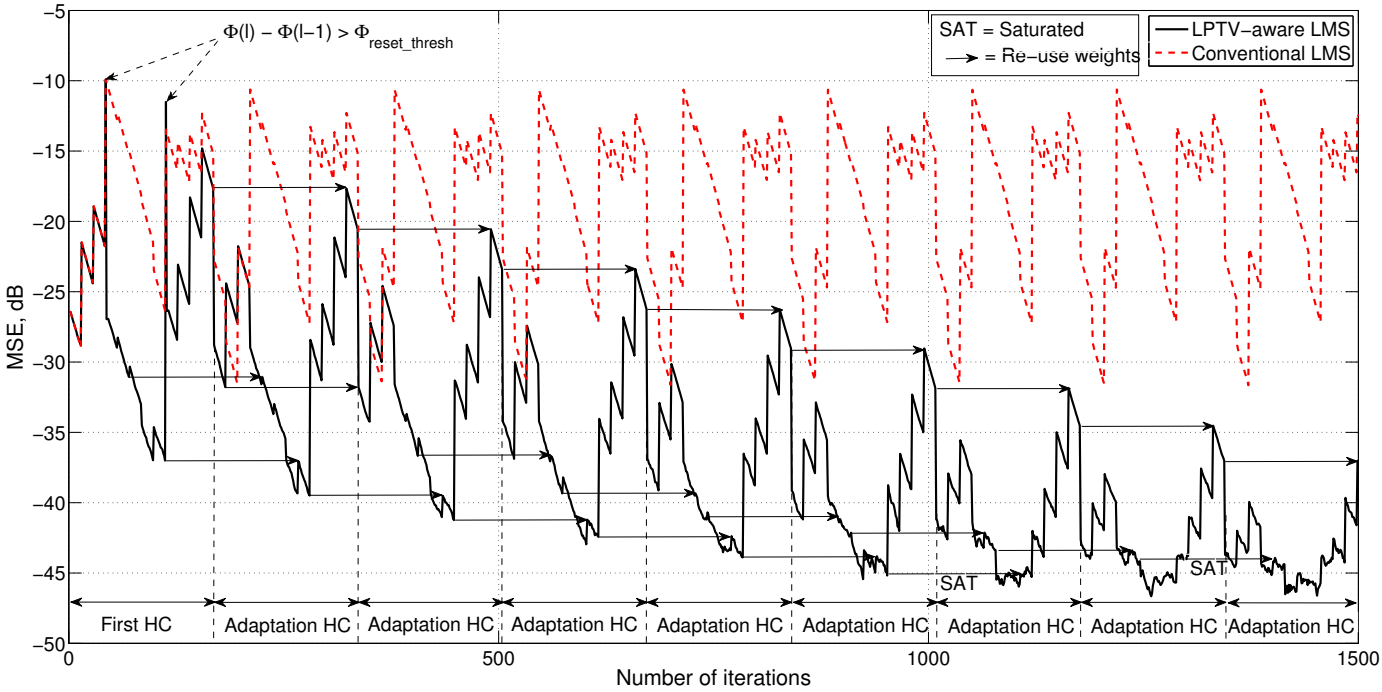


Fig. 7. MSE versus iteration number for MDEC using the conventional LMS and the proposed LPTV-aware LMS algorithms for an LPTV PLC channel. Total duration is nine HCs. LMS step size is $\mu = 0.025$.

$\frac{1}{\sqrt{2\pi}} \int_x^\infty \mathrm{e}^{-\frac{t^2}{2}} \mathrm{d}t$. From (15), we can observe that a decrease in SNR should be accompanied by a reduction in modulation order to maintain a constant target reliability. Therefore, for $\mathrm{SINR} \ll \mathrm{SNR}_{\mathrm{HD}}$, the overall data-rate gain (DRG) will be smaller than one, as the one-directional transmission rate for IBFD will be less than half of that of HD. For a range $\mathrm{SINR} \lesssim \mathrm{SNR}_{\mathrm{HD}}$, the loss in one-directional rate will be more than compensated by simultaneous bi-directional transmission and thus $1 \leq \mathrm{DRG} < 2$. Finally, for $\mathrm{SINR} \approx \mathrm{SNR}_{\mathrm{HD}}$, the full duplexing gain will be reaped and thus $\mathrm{DRG} = 2$. The region in which we lie depends on the EC gain (ECG)

$$\mathrm{ECG} = P_{\mathrm{TX}} - \max\{P_{\mathrm{RSI}}, N_{\mathrm{R}}, P_{\mathrm{QN}}\} \,. \tag{16}$$

### A. Echo Cancellation Gain

The exact value of ECG depends on the prevalent PLC channel conditions. In particular, as can be seen in (4), the received signal, which is used as a reference signal to update the LMS weights, consists of echo, SOI, and noise components. The latter two act as disturbance for the echo estimator. Hence, since the SOI component increases as the channel attenuation decreases, lower channel attenuation is expected to affect the accuracy of the SI estimate and thus the digital echo cancellation. Fig. 9 shows a scatter plot of the ECG from (16) (i.e., the gain from both the digital cancellation gain and the hybrid isolation) as a function of channel attenuation in OFDM sub-carriers. The results are obtained for 1000 randomly generated PLC channels using the simulator from [46] and the noise scenario as described in Appendix A-C. We observe that the ECG increases with increase in sub-carrier attenuation. We also observe from Fig. 9 that ECG saturates after a certain point, which is when the $P_{\mathrm{QN}}$ becomes dominant in (13).

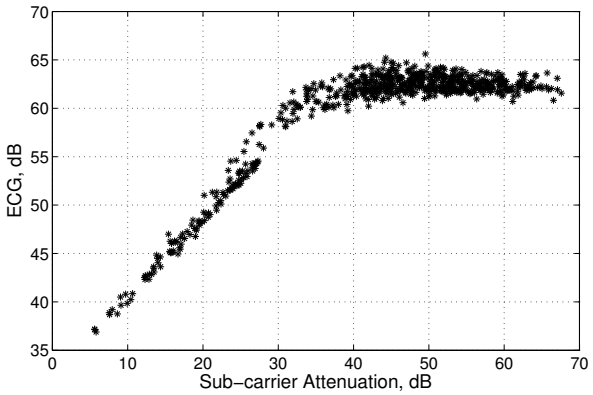


Fig. 9. Scatter plot of ECG as a function of sub-carrier attenuation. PLC sample channels generated with [46]. Noise scenario as described in Section III-C.

### B. Theoretical Data Rate Gains

We can now use the results from Fig. 9 to quantify the achievable DRGs, i.e., in which region of Fig. 8 we operate, as a function of the channel attenuation and noise level $N_{\mathrm{R}}$. This is presented in Table II, which shows the DRG as a function of the sub-carrier attenuation $\mathrm{SCA} = -20\log_{10}|H_{\mathrm{PLC},k}|$ and

TABLE II
DRG PER SUB-CARRIER AS A FUNCTION OF SUB-CARRIER CHANNEL ATTENUATION (SCA) AND CHANNEL NOISE LEVEL $N_{\mathrm{R}}$.

| | | $N_{\mathrm{R}}$ = -110 dBm/Hz | | | | | $N_{\mathrm{R}}$ = -130 dBm/Hz | | | | |
|---|---|---|---|---|---|---|---|---|---|---|---|
| SCA (dB) | ECG | $\mathrm{SNR}_{\mathrm{HD}}$ | $M_{\mathrm{HD}}$ | SINR | $M_{\mathrm{FD}}$ | DRG | $\mathrm{SNR}_{\mathrm{HD}}$ | $M_{\mathrm{HD}}$ | SINR | $M_{\mathrm{FD}}$ | DRG |
| 5 | 37 | 55 | 1024 | 32 | 1024 | 2 | 75 | 1024 | 32 | 1024 | 2 |
| 10 | 40 | 50 | 1024 | 30 | 256 | 1.6 | 70 | 1024 | 30 | 256 | 1.6 |
| 15 | 45 | 45 | 1024 | 30 | 256 | 1.6 | 65 | 1024 | 30 | 256 | 1.6 |
| 20 | 47 | 40 | 1024 | 27 | 256 | 1.6 | 60 | 1024 | 27 | 256 | 1.6 |
| 25 | 52 | 35 | 1024 | 27 | 256 | 1.6 | 55 | 1024 | 27 | 256 | 1.6 |
| 30 | 57 | 30 | 256 | 27 | 256 | 2 | 50 | 1024 | 27 | 256 | 1.6 |
| 35 | 59 | 25 | 64 | 24 | 64 | 2 | 45 | 1024 | 24 | 64 | 1.2 |
| 40 | 61 | 20 | 16 | 20 | 16 | 2 | 40 | 1024 | 21 | 64 | 1.2 |
| 45 | 62 | 15 | 16 | 15 | 16 | 2 | 35 | 1024 | 17 | 16 | <1 |
| 50 | 62 | 10 | 4 | 10 | 4 | 2 | 30 | 256 | 12 | 4 | <1 |
| 55 | 62 | 5 | 2 | 5 | 2 | 2 | 25 | 64 | 7 | 4 | <1 |
| 60 | 62 | 0 | 1 | 0 | 1 | N/A | 20 | 16 | 2 | 1 | <1 |

for two different noise levels. Depending on the resulting SNR and SINR values, we select constellation sizes $M_{\mathrm{HD}}$ and $M_{\mathrm{FD}}$ for the modulation scheme in conventional half-duplex and IBFD transmission, respectively. The modulation schemes are selected based on an adaptive modulation algorithm with $P_b^{\mathrm{t}} = 10^{-3}$ [4, Ch. 9]. We limit $\max(M_k) = 1024$, in accordance with the HPAV specifications [28].

For the relatively higher noise level of $N_{\mathrm{R}} = -110$ dBm/Hz, the values in Table II show that IBFD consistently provide DRGs, often at the maximum of a factor of two. For relatively low channel attenuation, i.e., $\mathrm{SCA} \lesssim 25$ dB, the DRG is diminished as $P_{\mathrm{RSI}}$ rises above the noise floor. However, in this region of operation, the SNR is very high and the rate of HD is limited by $\max(M_{\mathrm{HD},k})$. If the noise level is as low as $N_{\mathrm{R}} = -130$ dBm/Hz, then $P_{\mathrm{RSI}}$ and $P_{\mathrm{QN}}$ dominate the effective noise level $P_{\mathrm{eff}}$ (13) in IBFD, and we observe a DRG smaller than one for channels with high attenuation. If channel attenuation decreases, HD with practical signal constellations cannot further increase the rate due to increasing SNR, and IBFD becomes again beneficial in terms of achievable rate.

### C. Simulation Results of the Overall Date Rate Gain

The DRG values computed in the previous section correspond to individual sub-carriers experiencing a given sub-channel attenuation. In this section, we provide the overall DRG obtained across all OFDM sub-carriers of a channel.

*1) LPTV DRG Evolution:* We first consider an LPTV channel condition described in Appendix A-A1 and a low-noise scenario as explained in Appendix A-C and Table III, with the transceiver running our LPTV-LMS algorithm for EC. After every LPTV-LMS iteration, we calculate the overall DRG as

$$\mathrm{DRG} = \frac{2 \cdot \sum\limits_{k \in \mathscr{N}} \log_2(M_{\mathrm{FD},k})}{\sum\limits_{k \in \mathscr{N}} \log_2(M_{\mathrm{HD},k})}, \qquad (17)$$

where $\mathscr{N}$ is the set of all data carrying sub-carriers. The factor of two in the numerator in (17) accounts for the simultaneous bidirectional communication in IBFD. Fig. 10 shows the evolution of DRG with LPTV-LMS iterations for the three different step-sizes of $\mu = 0.025, 0.05, 0.075$. For completeness, we also show the MSE of the LMS algorithm in the same figure. As expected, we notice that the DRG convergence is fastest for the largest $\mu$. However, increase in $\mu$ also elevates the final MSE saturation value that affects the ECG, and in turn DRG. We find that $\mu = 0.05$ achieves a good trade-off between rate of convergence and final overall DRG. With $\mu = 0.05$, we observe that DRG convergences to its eventual value by about 900 iterations. This corresponds to 900 OFDM blocks, or a time duration of 45 ms for an extended OFDM block length of 50 $\mu$s [28, Table 4.2]. This duration is negligible when compared to the rate of N-CCC that a typical PLC network would experience. N-CCCs are caused by induced activities on the line, such as plugging in/out devices, or when there is a change in the state of operation of components connected to the line. Even on a busy in-home network, we do not expect such changes to occur more than, say, 20 per minute. This gives a worst-case transient period of $\frac{45\ ms}{3\ s} = 1.5\%$. We note that the results in Fig. 10 are for poor channel conditions of high attenuations. When channel attenuations are lower, Fig. 9 shows that the ECG is lower, indicating a higher saturated MSE. In such cases, the transient time is even lesser. Furthermore, we expect N-CCCs to occur much less frequently in a typical in-home power line network. Hence, we use the saturated value of ECG to evaluate DRGs for a larger set of channel conditions in the next section.

*2) Overall DRGs:* We now present results for the overall DRG obtained by running the IBFD system of Fig. 3(b) for a set of 1500 randomly generated channels and three different noise conditions as described in Appendix A-A2, and in Appendix A-C and Table III, respectively.

Fig. 11 shows the empirical CDF of the DRG from (17) for the three noise environments. We observe that the overall DRG is smaller than one only for less than 1% of the channels with our proposed IBFD solution even under relatively low noise conditions. For high noise levels, IBFD gives a minimum DRG of 1.6. Under medium noise conditions, IBFD is seen to consistently outperform conventional half-duplex rates to provide a median DRG of 76%.

## VI. Extension to MIMO BB-PLC Systems

In this section, we extend our IBFD solution to MIMO BB-PLC systems. MIMO BB-PLC has recently been standardized

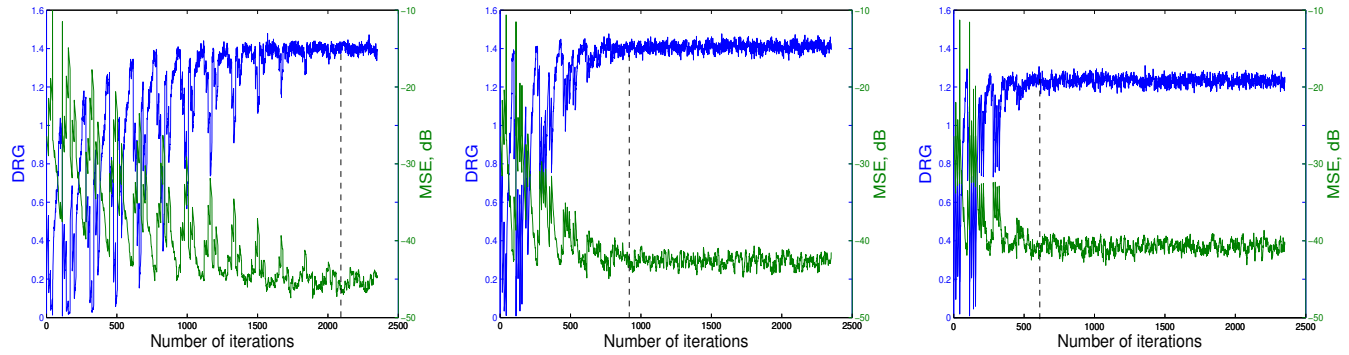


Fig. 10. DRG (overall increasing curves) and MSE (overall decreasing curves) versus iterations for LPTV-LMS with step-sizes of (a) $\mu = 0.025$, (b) $\mu = 0.05$, and (c) $\mu = 0.075$. Approximate DRG saturation points are shown by the dashed line.

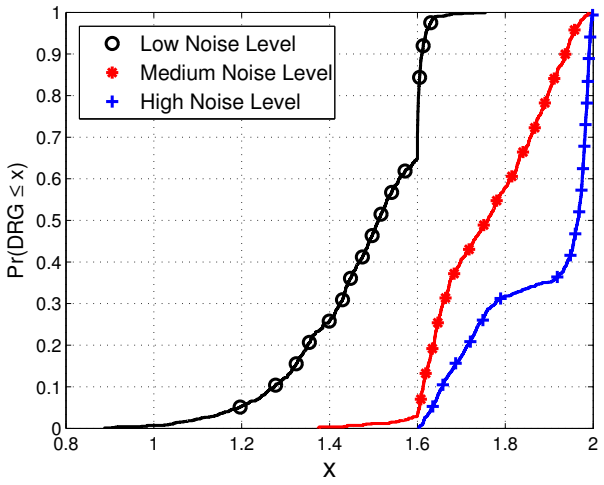


Fig. 11. Empirical CDF of overall DRG (17) using IBFD for a set of 1500 random channels under different noise conditions.

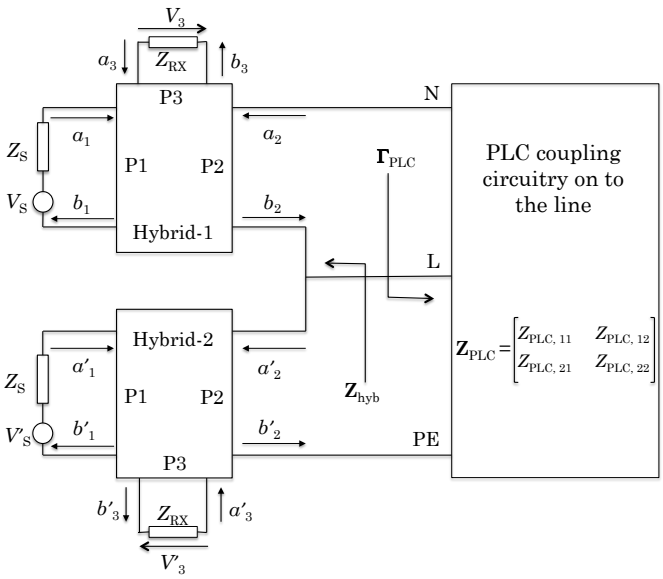


Fig. 12. Port connections of the active hybrids in a $2\times2$ MIMO configuration.

in the HomePlug AV2 and ITU-T G.9963 standards [5], [50] to enable data rates in the Gbps range. MIMO BB-PLC exploits the fact that often more than two conductors are available, which enables coupling of multiple input and decoupling of multiple output signals. The most common scenario is the use of three conductors, namely live or phase (L or P), neutral (N), and protective earth (PE), which enables a $2 \times 2$ MIMO system. This has been extended to a $2 \times 4$ setup, where a third differential signal and the common mode are included at the reception stage [4, Ch. 1]. We propose an IBFD solution for MIMO BB-PLC whose structure follows our two-step structure for the single-input single-output (SISO) case. In particular, we initially isolate the bidirectional signals in the analog domain and then cancel the remaining interference using a digital canceler.

### A. Analog Isolation

Fig. 12 shows the block diagram for the integration of the hybrids for analog isolation in a $2\times2$ MIMO BB-PLC system (we refer to [51, Fig. 12] [4, Ch. 1] for the schematic of a MIMO PLC coupler). As it can be seen, we require two 3-port hybrids, one at each transmit-end AFE. Each of these hybrids isolates the transmitted signal from the SOI on their pair of wires. If a $2 \times 4$ MIMO is being implemented, the other two reception modes use only the digital cancellation.

The amount of isolation provided by the hybrid depends on the extent of reflections caused due to impedance mismatch at the hybrid-line interface. The counterparts to reflection co-efficient $\Gamma_{\mathrm{PLC}}$, line impedance $Z_{\mathrm{PLC}}$, and hybrid output impedance $Z_2$ in the SISO system are the voltage reflection matrix $\boldsymbol{\Gamma}_{\mathrm{PLC}}$, the channel impedance matrix $\boldsymbol{Z}_{\mathrm{PLC}}$, and the dual-hybrid output impedance matrix $\boldsymbol{Z}_{\mathrm{hyb}}$, respectively, which are shown in Fig. 12. Since P1 and P3 of each of the hybrids are still connected to the transmit- and receive-end AFEs, respectively, we choose $Z_1 = Z_3 = 100\ \Omega$ for both the hybrids, following the analysis in Section III. $Z_2$ of each of the hybrids, which are the principal diagonal elements of $\boldsymbol{Z}_{\mathrm{hyb}}$, should be chosen in such a way that $\boldsymbol{\Gamma}_{\mathrm{PLC}}$ is kept at a minimum. Measurement results in [4, Chs. 1, 5]

indicate that the median impedance of typical MIMO channels between any two wire pairs is about 88 Ω. We also obtained some channel realizations from the open-source MIMO PLC channel generator tool [52] and found the impedance to be around 100 Ω. We thus conclude that $Z_2 = 100\ \Omega$ is still a good choice. Given these hybrid parameters and a channel impedance matrix $\boldsymbol{Z}_{\mathrm{PLC}}$, we can determine the SI and cross-interference (CI) channel frequency responses, $H_{ii}$ and $H_{ij}$, $i, j \in \{1, 2\}$, $i \neq j$, respectively, using an analysis similar to the SISO scenario. The details of the derivation are given in Appendix B-B.

### B. Digital Cancellation

We apply the previously validated mixed-domain digital cancellation procedure to a MIMO system by using two LMS filters at each transceiver, one to estimate the SI channel and the other for the CI channel. Fig. 13 illustrates the digital EC structure for canceling SI from the output of one of hybrids from Fig. 12. Denoting the two transmit signals of the MIMO system as $x_1$ and $x_2$, we can express the sampled output of the first hybrid as

$$y_1(n) = \underbrace{(x_1 * h_{11})(n)}_{\text{SI/self-echo}} + \underbrace{(x_2 * h_{12})(n)}_{\text{CI/cross-echo}} + \underbrace{y_{\mathrm{SOI}}(n)}_{\text{SOI}} + \underbrace{w(n)}_{\text{cumulative noise}}, \tag{18}$$

with the impulse responses $h_{11}$ and $h_{12}$ of the SI and CI channels, respectively. We note that the SOI usually contains components of two signals sent from the far-end transmitter, which is however irrelevant for the EC step. The SI and CI estimates are canceled simultaneously to produce a common error signal $e_1$. The LMS filters are updated in the frequency domain as

$$\boldsymbol{G}_{11}(\ell+1) = \boldsymbol{G}_{11}(\ell) + \mu \mathrm{diag}(\boldsymbol{X}_1(\ell))^* \boldsymbol{E}_1(\ell) \tag{19}$$

$$\boldsymbol{G}_{12}(\ell+1) = \boldsymbol{G}_{12}(\ell) + \mu \mathrm{diag}(\boldsymbol{X}_2(\ell))^* \boldsymbol{E}_1(\ell), \tag{20}$$

where $\boldsymbol{G}_{11}(\ell)$ and $\boldsymbol{G}_{12}(\ell)$ are the weights of the SI and CI estimation filters, respectively in the $\ell$th iteration, and $\boldsymbol{X}_1(\ell)$, $\boldsymbol{X}_2(\ell)$, and $\boldsymbol{E}_1(\ell)$ are the $\ell$th iteration frequency domain versions of $x_1$, $x_2$, and $e_1$, respectively. Similar adaptive cancellation is performed at the other transceiver path as well. When more than two receive modes are used, the same digital cancellation procedure is employed at the other receiver(s) to cancel the two CIs.

### C. Performance Results

For performance evaluation, we consider one of the two transceivers to determine the amount of SI and CI cancellation achieved by the EC solution described in Fig. 13. We operate under the same system settings and noise conditions reported in Section V, while we generate MIMO channels as specified in Appendix A-B.

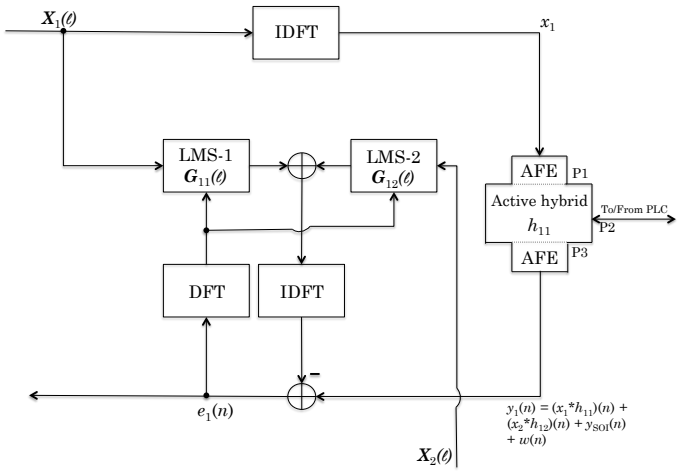


Fig. 13. Block diagram for digital EC for one received signal in an IBFD enabled MIMO transceiver.

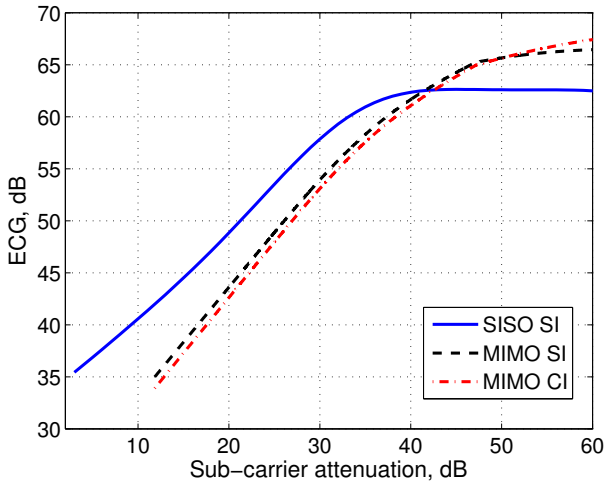


Fig. 14. Total ECG for SI and CI with respect to SI ECG for SISO.

*1) Echo Cancellation Gains:* For the MIMO BB-PLC case, interference is caused by both SI and CI. Hence, we define $\mathrm{ECG}_{\mathrm{SI}}$ and $\mathrm{ECG}_{\mathrm{CI}}$ as the ECG obtained for SI and CI, respectively, which are given by

$$\mathrm{ECG}_{\mathrm{SI}} = P_{\mathrm{TX}} - \max\{P_{\mathrm{RSI}}, N_{\mathrm{R}}, P_{\mathrm{QN}}\} \tag{21}$$

$$\mathrm{ECG}_{\mathrm{CI}} = P_{\mathrm{TX}} - \max\{P_{\mathrm{RCI}}, N_{\mathrm{R}}, P_{\mathrm{QN}}\}\ , \tag{22}$$

where $P_{\mathrm{RCI}}$ is the PSD of the residual CI. Fig. 14 shows the smoothing spline curve-fit data for $\mathrm{ECG}_{\mathrm{SI}}$ and $\mathrm{ECG}_{\mathrm{CI}}$ for 1000 different channel realizations, in comparison to the ECG obtained in SISO operation. We notice that $\mathrm{ECG}_{\mathrm{SI}}$ and $\mathrm{ECG}_{\mathrm{CI}}$ show the same trend as the SISO ECG with gains increasing with higher sub-carrier attenuations. We also observe that $\mathrm{ECG}_{\mathrm{SI}} \approx \mathrm{ECG}_{\mathrm{CI}}$ across all sub-carriers. However, the specific gain values deviate from the ECG for the SISO case. This is due to a larger pre-digital attenuation of the SI signal. In particular, the multi-conductor line-hybrid interface provides an average of 12 dB of isolation in the MIMO scenario as opposed to 7 dB of average isolation seen in the SISO case. This higher isolation results in lower SI

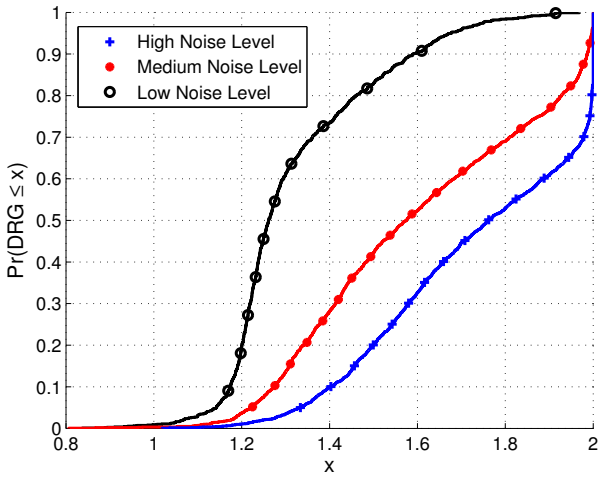


Fig. 15. Empirical CDF of overall MIMO DRG (17) using IBFD for a set of 1500 random channels under different noise conditions.

and CI strengths entering the LMS estimator. Under low sub-carrier attenuations, this leads to a smaller difference between the signal strengths of SI/CI and SOI, which produces less accurate SI/CI estimates, leading to lower digital cancellation gains. As the sub-carrier attenuation increases, the difference between the signal strengths increases. This produces higher digital cancellation gain, which when combined with a greater pre-digital isolation produces a larger overall MIMO ECG.

*2) Overall Data Rate Gains:* We measure the DRG as defined in (17) for 1500 randomly generated MIMO channels (see Appendix A-B). The empirical CDF of the DRG is shown in Fig. 15 for the three different noise levels described in Appendix A-C and Table III. We observe that in almost all cases, the DRG is larger than one for all three noise conditions. However, the DRGs are generally lower than those for the SISO case. The reason for this is the lower ECG values for relatively smaller sub-carrier attenuations as shown in Fig. 14. We obtain a median DRG of about 1.6 under typical (medium) noise conditions and nearly double the data rates for 20% of the cases under high noise levels.

## VII. Conclusion

In this paper, we have considered the application of IBFD for BB-PLC as a means to significantly enhance data rates under typical channel and noise conditions and to solve several prevalent networking problems. We have motivated and developed a two-step implementation, consisting of an active hybrid to provide initial analog isolation and a mixed-domain digital echo cancellation for effective self-interference reduction. Furthermore, we have addressed the problem of LPTV channel behavior typically seen in PLC, by developing a new LPTV-aware LMS adaptation algorithm, which exploits the cyclic nature of the channel changes to provide better error convergence and more accurate echo channel estimates. We have also extended our solution for application in MIMO BB-PLC systems. The presented quantitative results suggest that our IBFD solution provides significant data rate gains over conventional time-division duplexed BB-PLC transmission for a range of channel and noise scenarios. The proposed IBFD scheme can be readily integrated into the existing half-duplex systems and also ensures interoperability with the non-upgraded half-duplex devices. The enhancement of cancellation gains through the addition of an ACC component is an interesting future work.

## Appendix A
## Channel and Noise Models

### A. SISO Channel Generation

To generate SISO PLC channels, we use the open-source channel generator tool [46], which implements the bottom-up approach from [53][5]. It allows us to choose different network conditions for an in-home setting by assigning the number of derivation boxes (DB), number of outlets (OL) associated with each box, the cable types and lengths, and the loads connected at each of the OL. It also provides an option to generate a random network topology in which it automatically creates an in-home network setting by randomly choosing the above parameters.

*1) LPTV Channels:* To generate an LPTV channel condition, we consider an in-home scenario with harmonic and commuted load variations at some of the OLs in the network [48]. The indoor topology that we have selected for the results in this paper consists of 25 OLs, of which 7 are without any load, each 5 are connected to commuted and to harmonically varying loads that are both resistive and frequency-selective in nature, and the remaining 8 are connected to other time invariant resistive and frequency-selective loads. We consider a minimum channel coherence time of $T_c = 700$ $\mu$s for in-home power lines, as reported in [29]. For North American mains frequency of 60 Hz, this results in $\frac{1}{60 \cdot 2 \cdot 700 \cdot 10^{-6}} = 12$ channel changes in one HC. We therefore generate 12 time invariant channels and switch from one to the other after every $T_c$. We apply this in every HC to replicate the LPTV behavior in an actual PLC setting. These 12 channels have a minimum and maximum sub-carrier attenuations of 30 dB and 78 dB, respectively, with a mean of about 53 dB for the selected network setting.

*2) Channels to Determine DRG:* For generating a large set of channels, we use the random network generator setting in [46]. We limit the maximum number of DBs and OLs to 15 each to simulate a realistic in-home network. With such a setting, we obtain channels with sub-carrier attenuations varying between 6 dB to 77 dB with a mean of 40 dB. The statistics of the channel frequency responses generated using [46] have been shown to closely match those from [48] whose average coherence bandwidth is about 200 kHz.

### B. MIMO Channel Generation

To generate a set of 1500 random MIMO channels, we use the channel generator tool of [52]. To simulate a realistic in-

[5]We note that a bottom-up approach is required for the performance evaluation of the proposed IBFD method, as it provides realizations for the frequency response together with the associated access impedance. This would not be the case using phenomenological descriptions for the channel frequency response as provided in e.g. [54]–[56].

home network setting, we lay a tree topology of 15 outlet nodes and 20 branches, and vary the branch lengths from 1 to 100 meters, and different loads conditions at each outlet varying between 1 Ω to 2 kΩ. We also vary the backbone conductor with the two available options of symmetric and ribbon-type cables. This results in channels with sub-carrier attenuations varying between 10 dB and 70 dB with a mean of 42 dB.

### C. PLC Noise Generation

We consider the PLC noise as a sum of background, narrowband, and impulse noise, as described in [57, Annex. F][6]. The former two can be assumed stationary and are described through their PSDs.

*1) Colored Background Noise:* The PSD for the colored background noise is modeled as a first order exponential,

$$S(f) = a + b|f|^c, \tag{23}$$

where $a$, $b$, and $c$ can be varied for different noise conditions, as specified in Table III.

*2) Narrowband Noise:* The narrowband noise PSD follows a parametric Gaussian function. We do not vary narrowband noise parameters for different noise levels as they are typically independent of the network conditions and are usually introduced by interfering short-wave or amateur radio signals.

*3) Impulse Noise:* The impulse noise is generated in time domain using the sum-of-sinusoids model,

$$p(t) = (u(t) - u(t - T_d)) \cdot \sum_{i=0}^{N_d - 1} \frac{A_i}{N_d} \mathrm{e}^{-\alpha_i |t|} \mathrm{e}^{-j2\pi f_i t},$$

where $u(\cdot)$ is the unit step function, $N_d$ is the number of damped sinusoids in an impulse, $T_d$ is the duration of the impulse, $A_i$ is the impulse amplitude, and $\alpha_i$ and $f_i$ are the damping factor and pseudo frequency of the $i$th sinusoid, respectively. We generate $N_T$ such impulses for every mains cycle, spread by an inter-arrival time, $t_{\text{int}}$. $N_d = 3$ and $\alpha_i = 0.3 \times 10^6$ are fixed, and other parameters are adjusted to generate different types of impulse noise, namely periodic synchronous (PS), periodic asynchronous (PA), and aperiodic (AP) impulse noise, and to account for different noise levels specified in [61], as shown in Table III.

To enable reproducibility of our experiments, we have made the noise generator available online [62].

TABLE III
NOISE STATISTICS USED TO GENERATE THE DIFFERENT NOISE LEVELS

| | High | Medium | Low |
|---|---|---|---|
| $f_i$ (MHz) | | | |
| PS | $\mathcal{U}$[0.25, 0.5] | $\mathcal{U}$[0.25, 0.5] | $\mathcal{U}$[0.25, 0.5] |
| PA | $\mathcal{U}$[2, 13] | $\mathcal{U}$[2, 13] | $\mathcal{U}$[2, 13] |
| AP | $\mathcal{U}$[0.5, 1] | $\mathcal{U}$[0.5, 1] | $\mathcal{U}$[0.5, 1] |
| $T_d(\mu s)$ | | | |
| PS | 300 | $\mathcal{U}$[2,300] | 2 |
| PA | 10 | $\mathcal{U}$[1.5, 10] | 1.5 |
| AP | 150 | $\mathcal{U}$[15, 150] | 15 |
| $A_i$ (mV) | | | |
| PS | 1500 | $\mathcal{U}$[5, 1500] | 5 |
| PA | 40 | $\mathcal{U}$[4, 40] | 4 |
| AP | 150 | $\mathcal{U}$[5, 150] | 5 |
| $t_{\text{int}}$ (ms) | | | |
| PS | $\mathcal{U}$[10, 200] | $\mathcal{U}$[10, 200] | $\mathcal{U}$[10, 200] |
| PA | $\mathcal{U}$[10, 200] | $\mathcal{U}$[10, 200] | $\mathcal{U}$[10, 200] |
| AP | $\mathcal{E}(\lambda^{-1} = 100)$ | $\mathcal{E}(\lambda^{-1} = 100)$ | $\mathcal{E}(\lambda^{-1} = 100)$ |
| $N_T$ | | | |
| PS | 10 | $\mathcal{U}$[1, 10] | 1 |
| PA | 5 | $\mathcal{U}$[0, 5] | 0 |
| AP | 10 | $\mathcal{U}$[1, 10] | 1 |
| $S(f)$ (dBm/Hz) | | | |
| $a$ | -145 | $\mathcal{U}$[-140, -145] | -140 |
| $b$ | 53.23 | $\mathcal{U}$[52.23, 38.75] | 38.75 |
| $c$ | -0.337 | $\mathcal{U}$[-0.337, -0.72] | -0.72 |

$\mathcal{U}[z_1, z_2]$ denotes a random number that is drawn from a uniform distribution between $z_1$ and $z_2$.
$\mathcal{E}[\lambda^{-1} = \lambda_0]$ denotes a random number drawn from an exponential distribution with mean of $\lambda_0$.

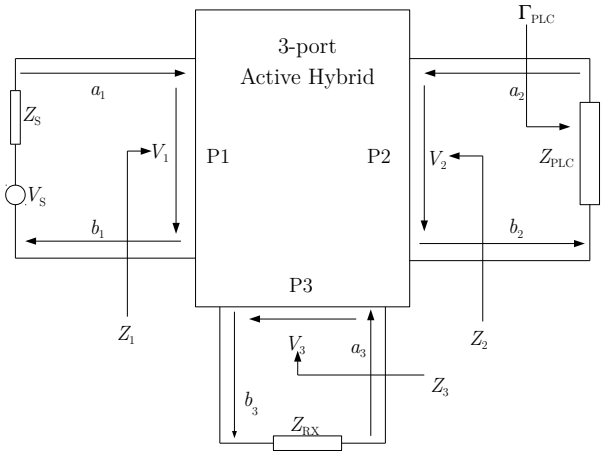


Fig. 16. Port connections of the active hybrid in SISO configuration.

## APPENDIX B
## TRANSFER FUNCTION OF THE ECHO CHANNELS

### A. Self-Interference Channel in SISO IBFD Operation

We consider the SISO-IBFD scenario illustrated in Fig. 16 to derive an expression for the echo channel transfer function $H_{\text{SI}}(f) = \frac{V_3(f)}{V_{\text{S}}(f)}$ for a given frequency $f$. For brevity, we do not include the frequency-dependency in the following. We first express $H_{\text{SI}}$ in terms of the S-parameters of the hybrid and then represent the S-parameters in terms of the outward reflection coefficient at P2 ($\Gamma_{\text{PLC}}$). To this end, we terminate P2 with impedance $Z_{\text{PLC}}$ and view the hybrid as a 2-port network between P1 and P3. With a reference impedance $Z_0$ at P1 and P3, we obtain $H_{\text{SI}}$ from the S-parameters as [63, Ch. 3]

$$H_{\text{SI}} = \frac{V_3}{V_{\text{S}}} = \frac{S_{21}(1 + \Gamma_{\text{L}})(1 - \Gamma_{\text{S}})}{2(1 - S_{22}\Gamma_{\text{L}})(1 - \Gamma_{\text{in}}\Gamma_{\text{S}})}, \tag{24}$$

[6]The noise model described in the IEEE standard document [57] is the result of studies over many years published in e.g. [33], [58], [59]. We note that especially noise models can vary for different scenarios. For example, [60] reports a set of measurements suggesting a non-Gaussian background noise.

where

$$\Gamma_{\text{in}} = S_{11} + \frac{S_{12}S_{21}\Gamma_{\text{L}}}{1 - S_{22}\Gamma_{\text{L}}}$$
$$\Gamma_{\text{S}} = \frac{Z_{\text{S}} - Z_0}{Z_{\text{S}} + Z_0}$$
$$\Gamma_{\text{L}} = \frac{Z_{\text{RX}} - Z_0}{Z_{\text{RX}} + Z_0}.$$

Our modified hybrid circuit of Fig. 1 has no transfer connection from P3 to P1, which results in $S_{12} = 0$ due to the reverse isolation of the op-amps. This results in $\Gamma_{\text{in}} = S_{11}$. Therefore,

$$H_{\text{SI}} = \frac{S_{21}(1+\Gamma_{\text{L}})(1-\Gamma_{\text{S}})}{2(1 - S_{22}\Gamma_{\text{L}})(1 - S_{11}\Gamma_{\text{S}})} = c \cdot S_{21} \ , \tag{25}$$

where $c = \frac{(1+\Gamma_{\text{L}})(1-\Gamma_{\text{S}})}{2(1-S_{22}\Gamma_{\text{L}})(1-S_{11}\Gamma_{\text{S}})}$.

Next, we represent $S_{21}$ in terms of $\Gamma_{\text{PLC}}$. By definition we have,

$$S_{21} = \left.\frac{b_3}{a_1}\right|_{a_3=0} \tag{26}$$

$$\Gamma_{\text{PLC}} = \frac{a_2}{b_2} \ , \tag{27}$$

where $a_i$ and $b_i$ are the inward and outward traveling waves of the hybrid, respectively. The amplifier and voltage divider stages and the reverse isolation of the op-amps used in the hybrid ensure that the signal entering one port is completely transferred to the next [39], resulting in

$$b_2 = a_1 \tag{28}$$

$$b_3 = a_2 \ . \tag{29}$$

From (27)-(29) it follows that

$$\frac{b_3}{a_1} = \frac{b_3}{b_2} = \frac{a_2\Gamma_{\text{PLC}}}{a_2} = \Gamma_{\text{PLC}} \ . \tag{30}$$

Finally, combining (25), (26), and (30), we have,

$$H_{\text{SI}} = c \cdot \Gamma_{\text{PLC}} \ . \tag{31}$$

The factor $c$ depends on $\Gamma_{\text{L}}$, $\Gamma_{\text{S}}$, $S_{11}$, and $S_{22}$. Without loss of generality, we choose reference impedance $Z_0 = 100\ \Omega$, which results in $\Gamma_{\text{L}} = 0$. On the other hand, $Z_{\text{S}}$ is typically low [42], and gives $\Gamma_{\text{S}} \approx -1$. The values of $S_{11}$ and $S_{22}$ are independent of $Z_{\text{PLC}}$, and only depend on $Z_1$, $Z_2$, $Z_{\text{S}}$, $Z_{\text{RX}}$, and $Z_0$. Furthermore, since these impedances are purely resistive, $S_{11}$ and $S_{22}$ are also frequency independent. ADS simulations of our circuit in Fig. 1 indicate $S_{11} = S_{22} = 0.1$ for the given $Z_1$, $Z_2$, $Z_{\text{S}}$, $Z_{\text{RX}}$, and $Z_0$. With these values, we obtain $c = 0.9$ for our hybrid.

### *B. Self- and Cross-Interference Channels in MIMO-IBFD Operation*

We consider the block diagram for a $2 \times 2$ MIMO PLC system in Fig. 12. The voltage reflection matrix $\mathbf{\Gamma}_{\text{PLC}}$ is calculated as [64, Ch. 7]

$$\mathbf{\Gamma}_{\text{PLC}} = \begin{bmatrix} \Gamma_{11} & \Gamma_{12} \\ \Gamma_{21} & \Gamma_{22} \end{bmatrix} = [\boldsymbol{Z}_{\text{PLC}} - \boldsymbol{Z}_{\text{hyb}}][\boldsymbol{Z}_{\text{PLC}} + \boldsymbol{Z}_{\text{hyb}}]^{-1}.$$

We first study SI on Hybrid-1 (see Fig. 12). Following the same approach as for the SISO case in Appendix B-A, we view the hybrid as a 2-port network with ports P1 and P3 as the two ports. From the derivation in Appendix B-A, we obtain the SI channel transfer function

$$H_{11} = \frac{V_3}{V_{\text{S}}} = c_{11}\Gamma_{11} \ , \tag{32}$$

where $c_{11} = \frac{(1+\Gamma_{\text{L}})(1-\Gamma_{\text{S}})}{2(1-S_{22}\Gamma_{\text{L}})(1-S_{11}\Gamma_{\text{S}})}$ and $S_{ij}$ are the S-parameters of Hybrid-1.

We extend this analysis further to the CI channel from transmitter 2 to receiver 1, i.e., P1 of Hybrid-2 and P3 of Hybrid-1 are the two ports. Considering the signal definitions in Fig. 12 and analogous to (27) and (28), we now have

$$a_2 = \Gamma_{12} b_2' \tag{33}$$

$$b_2' = a_1' \ . \tag{34}$$

From (29), (33), and (34), we obtain

$$\frac{b_3}{a_1'} = \frac{b_3}{b_2'} = \frac{a_2}{b_2'} = \frac{\Gamma_{12}b_2'}{b_2'} = \Gamma_{12} \tag{35}$$

and thus

$$H_{12} = \frac{V_3}{V_{\text{S}}'} = c_{12} \cdot \Gamma_{12} \ , \tag{36}$$

where $c_{12} = \frac{(1+\Gamma_{\text{L}})(1-\Gamma_{\text{S}})}{2(1-S_{22}\Gamma_{\text{L}})(1-S_{11}\Gamma_{\text{S}})}$. Following the same analysis leads to the SI and CI channel observed at Hybrid-2,

$$H_{21} = \frac{V_3'}{V_{\text{S}}} = c_{21} \cdot \Gamma_{21} \tag{37}$$

$$H_{22} = \frac{V_3'}{V_{\text{S}}'} = c_{22} \cdot \Gamma_{22} \ , \tag{38}$$

where we replace the S-parameters from the Hybrid-1 with those from Hybrid-2 to compute the constants $c_{21}$ and $c_{22}$.

## REFERENCES

[1] G. Prasad, L. Lampe, and S. Shekhar, "Enhancing transmission efficiency in broadband PLC systems with in-band full duplexing," in *IEEE Intl. Symp. Power Line Commun. and its Appl. (ISPLC)*, 2016.

[2] H. Hrasnica, A. Haidine, and R. Lehnert, *Broadband powerline communications: network design*. John Wiley & Sons, 2005.

[3] L. Lampe, A. M. Tonello, and T. G. Swart, *Power Line Communications: Principles, Standards and Applications from Multimedia to Smart Grid*. John Wiley & Sons, 2016.

[4] L. T. Berger, A. Schwager, P. Pagani, and D. Schneider, *MIMO Power Line Communications: Narrow and Broadband Standards, EMC, and Advanced Processing*. CRC Press, 2014.

[5] L. Yonge, J. Abad, K. Afkhamie, L. Guerrieri, S. Katar, H. Lioe, P. Pagani, R. Riva, D. M. Schneider, and A. Schwager, "An overview of the homeplug AV2 technology," *J. of Elect. and Comput. Eng.*, 2013.

[6] Y.-S. Choi and H. Shirani-Mehr, "Simultaneous transmission and reception: Algorithm, design and system level performance," *IEEE Trans. Wireless Commun.*, vol. 12, no. 12, pp. 5992–6010, 2013.

[7] B. Praho, M. Tlich, P. Pagani, A. Zeddam, and F. Nouvel, "Cognitive detection method of radio frequencies on power line networks," in *IEEE Intl. Symp. Power Line Commun. and its Appl. (ISPLC)*, 2010, pp. 225–230.

[8] S. Weinstein, "Echo cancellation in the telephone network," *IEEE Commun. Mag.*, vol. 15, no. 1, pp. 8–15, January 1977.

[9] M. Sondhi and D. A. Berkley, "Silencing echoes on the telephone network," *Proc. of the IEEE*, vol. 68, no. 8, pp. 948–963, Aug 1980.

[10] M. Ho, J. M. Cioffi, and J. A. Bingham, "Discrete multitone echo cancelation," *IEEE Trans. Commun.*, vol. 44, no. 7, pp. 817–825, 1996.

[11] N. Verhoeckx, H. Van Den Elzen, F. Snijders, and P. Van Gerwen, "Digital echo cancellation for baseband data transmission," *IEEE Trans. Acoust., Speech, Signal Process.*, vol. 27, no. 6, pp. 768–781, 1979.

[12] W. Y. Chen, J. L. Dixon, and D. L. Waring, "High bit rate digital subscriber line echo cancellation," *IEEE J. Sel. Areas Commun.*, vol. 9, no. 6, pp. 848–860, 1991.

[13] F. Lindqvist and A. Fertner, "Frequency Domain Echo Canceller for DMT-Based Systems," *IEEE Signal Process. Lett.*, vol. 18, no. 12, pp. 713–716, 2011.

[14] N. Ehtiati and B. Champagne, "Constrained adaptive echo cancellation for discrete multitone systems," *IEEE Trans. Signal Process.*, vol. 57, no. 1, pp. 302–312, 2009.

[15] K. Van Acker, M. Moonen, and T. Pollet, "Per-tone echo cancellation for DMT-based systems," *IEEE Trans. Commun.*, vol. 51, no. 9, pp. 1582–1590, 2003.

[16] R. Mahadevan, "A front-end circuit for full-duplex transmission over coaxial cable." Ph.D. dissertation, University of Toronto, 2001.

[17] N. Ehtiati and B. Champagne, "A general framework for mixed-domain echo cancellation in discrete multitone systems," *IEEE Trans. Commun.*, vol. 61, no. 2, pp. 769–780, 2013.

[18] T.-C. Lee and B. Razavi, "A 125-MHz mixed-signal echo canceller for gigabit ethernet on copper wire," *IEEE J. Solid-State Circuits*, vol. 36, no. 3, pp. 366–373, 2001.

[19] R. Farjad, F. Gerfers, M. Brown, A. R. Tavakoli, D. Nguyen, H. Sedarat, R. Shirani, and H.-T. Ng, "A 48-Port FCC-Compliant 10GBASE-T Transmitter With Mixed-Mode Adaptive Echo Canceller," *IEEE J. Solid-State Circuits*, vol. 47, no. 12, pp. 3261–3272, 2012.

[20] D. Bharadia, E. McMilin, and S. Katti, "Full duplex Radios," in *ACM SIGCOMM*, 2013, pp. 375–386.

[21] A. Sabharwal, P. Schniter, D. Guo, D. W. Bliss, S. Rangarajan, and R. Wichman, "In-band full-duplex wireless: Challenges and opportunities," *IEEE J. Sel. Areas Commun.*, vol. 32, no. 9, pp. 1637–1652, 2014.

[22] J. I. Choi, M. Jain, K. Srinivasan, P. Levis, and S. Katti, "Achieving single channel, full duplex wireless communication," in *ACM MOBICOM*, 2010, pp. 1–12.

[23] M. Duarte, C. Dick, and A. Sabharwal, "Experiment-driven characterization of full-duplex wireless systems," *IEEE Trans. Wireless Commun.*, vol. 11, no. 12, pp. 4296–4307, 2012.

[24] M. Jain, J. I. Choi, T. Kim, D. Bharadia, S. Seth, K. Srinivasan, P. Levis, S. Katti, and P. Sinha, "Practical, real-time, full duplex wireless," in *ACM MOBICOM*, 2011, pp. 301–312.

[25] "IEC 62488-1:2012: Power line communication systems for power utility applications," *International Electrotechnical Commission*. [Online]. Available: https://webstore.iec.ch/

[26] C. Tripodi, G. Ferrari, R. Pighi, and R. Raheli, "Echo cancellation in a power line modem in the presence of abrupt channel variations," in *IEEE Intl. Symp. Power Line Commun. and its Appl. (ISPLC)*, 2014, pp. 208–213.

[27] ——, "A novel weight reset strategy for the LMS algorithm subject to abrupt channel variations," in *IEEE Intl. Symp. Power Line Commun. and its Appl. (ISPLC)*, 2015, pp. 131–136.

[28] H. A. Latchman, S. Katar, L. Yonge, and S. Gavette, *Homeplug AV and IEEE 1901: A Handbook for PLC Designers and Users*. Wiley-IEEE Press, 2013.

[29] F. J. Cañete, J. A. Cortés, L. Díez, and J. T. Entrambasaguas, "Analysis of the cyclic short-term variation of indoor power line channels," *IEEE J. Sel. Areas Commun.*, vol. 24, no. 7, pp. 1327–1338, 2006.

[30] D. Benyoucef, "A new statistical model of the noise power density spectrum for powerline communication," in *IEEE Intl. Symp. on Power Line Commun. and its Appl. (ISPLC)*, 2003, pp. 136–141.

[31] H. B. Çelebi, "Noise and multipath characteristics of power line communication channels," Master's thesis, University of South Florida, 2010.

[32] T. Esmailian, F. Kschischang, and P. Gulak, "Characteristics of in-building power lines at high frequencies and their channel capacity," in *IEEE Intl. Symp. Power Line Commun. and its Appl. (ISPLC)*, 2000, pp. 52–59.

[33] ——, "In-building power lines as high-speed communication channels: channel characterization and a test channel ensemble," *Int. J. Commun. Syst.*, vol. 16, no. 5, pp. 381–400, 2003.

[34] J. O'Reilly, *Telecommunications Principles*. Springer Science & Business Media, 1989, vol. 5.

[35] D. Dardari, "Joint clip and quantization effects characterization in OFDM receivers," *IEEE Trans. Circuits Syst. I: Regular Papers*, vol. 53, no. 8, pp. 1741–1748, 2006.

[36] H. Ehm, S. Winter, and R. Weigel, "Analytic quantization modeling of OFDM signals using normal Gaussian distribution," in *Asia-Pacific Microwave Conference*, Dec 2006, pp. 847–850.

[37] Intersil ISL1571 datasheet. [Online]. Available: http://www.intersil.com/content/dam/Intersil/documents/isl1/isl1571.pdf

[38] L. Laughlin, M. Beach, K. Morris, J. L. Haine *et al.*, "Electrical balance duplexing for small form factor realization of in-band full duplex," *IEEE Commun. Mag.*, vol. 53, no. 5, pp. 102–110, 2015.

[39] C. Wenzel, "Low frequency circulator/isolator uses no ferrite or magnet," *RF Design (1991)*, pp. 39–43.

[40] W.-K. Su, Y.-R. Chen, and D. Lin, "Optimization of hybrid circuits for echo cancellation in high-rate digital subscriber line transmission," in *IEEE Asia-Pacific Conference on Circuits and Systems (APCCAS)*, Dec 1994, pp. 334–339.

[41] N. Taherinejad, L. Lampe, and S. Mirabbasi, "Adaptive impedance matching for vehicular power line communication systems," in *IEEE Intl. Symp. Power Line Commun. and its Appl. (ISPLC)*, 2014, pp. 214–219.

[42] Maxim. Integrated powerline communication analog front-end transceiver and line driver. [Online]. Available: http://www.maximic.com/datasheet/index.mvp/id/6333

[43] S. S. Haykin, *Adaptive filter theory*. Pearson Education India, 2007.

[44] C. Temperton, "A generalized prime factor FFT algorithm for any N=2^p3^q5^r," *SIAM J. on Scientific and Statistical Computing*, vol. 13, no. 3, pp. 676–686, 1992.

[45] M. Arnao and S. Rao, "A variable-step LMS based on tap weight time variation," in *International Conference on Acoustics, Speech, and Signal Processing (ICASSP)*, 1990, pp. 1453–1456.

[46] G. Marrocco, D. Statovci, and S. Trautmann, "A PLC broadband channel simulator for indoor communications," in *IEEE Intl. Symp. Power Line Commun. and its Appl. (ISPLC)*, 2013, pp. 321–326.

[47] LMH6628 dual wideband, low noise, voltage feedback op amp. [Online]. Available: http://www.ti.com/lit/ds/symlink/lmh6628.pdf

[48] F. J. Canete, J. Cortés, L. Díez, and J. T. Entrambasaguas, "A channel model proposal for indoor power line communications," *IEEE Commun. Mag.*, vol. 49, no. 12, pp. 166–174, 2011.

[49] S. T. Chung and A. J. Goldsmith, "Degrees of freedom in adaptive modulation: a unified view," *IEEE Trans. Commun.*, vol. 49, no. 9, pp. 1561–1571, 2001.

[50] International Telecommunications Union (ITU), "ITU-T Recommendation G.9963, Unified high-speed wire-line based home networking transceivers - Multiple Input/Multiple Output (MIMO)," Sep. 2011, (ex G.hn-MIMO).

[51] ETSITR101562v1.1.1, "PowerLine Telecommunications (PLT) MIMO PLT Universal Coupler, Operating Instructions - Description," European Telecommunications Standards Institute, Tech. Rep., 2011.

[52] F. Gruber and L. Lampe, "On PLC channel emulation via transmission line theory," in *IEEE Intl. Symp. Power Line Commun. and its Appl. (ISPLC)*, Austin, TX, USA, 2015. [Online]. Available: http://www.ece.ubc.ca/~lampe/MIMOPLC

[53] A. M. Tonello and F. Versolatto, "Bottom-up statistical PLC channel modeling—Part I: Random topology model and efficient transfer function computation," *IEEE Trans. Power Del.*, vol. 26, no. 2, pp. 891–898, 2011.

[54] I. C. Papaleonidopoulos, C. N. Capsalis, C. G. Karagiannopoulos, and N. J. Theodorou, "Statistical analysis and simulation of indoor single-phase low voltage power-line communication channels on the basis of multipath propagation," *IEEE Trans. Consum. Electron.*, vol. 49, no. 1, pp. 89–99, 2003.

[55] S. Guzelgoz, H. B. Çelebi, and H. Arslan, "Statistical characterization of the paths in multipath PLC channels," *IEEE Trans. Power Del.*, vol. 26, no. 1, pp. 181–187, 2011.

[56] S. Galli, "A novel approach to the statistical modeling of wireline channels," *IEEE Trans. Commun.*, vol. 59, no. 5, pp. 1332–1345, 2011.

[57] "IEEE standard for broadband over power line networks: Medium access control and physical layer specifications," *IEEE Std 1901-2010*, pp. 1–1586, Dec 2010.

[58] M. Zimmermann and K. Dostert, "Analysis and modeling of impulsive noise in broad-band powerline communications," *IEEE Trans. Electromagn. Compat.*, vol. 44, no. 1, pp. 249–258, 2002.

[59] V. Degardin, M. Lienard, A. Zeddam, F. Gauthier, and P. Degauquel, "Classification and characterization of impulsive noise on indoor powerline used for data communications," *IEEE Trans. Consum. Electron.*, vol. 48, no. 4, pp. 913–918, 2002.

[60] H. Meng, Y. L. Guan, and S. Chen, "Modeling and analysis of noise effects on broadband power-line communications," *IEEE Trans. Power Del.*, vol. 20, no. 2, pp. 630–637, 2005.

[61] J. A. Cortés, L. Díez, F. J. Cañete, and J. J. Sánchez-Martínez, "Analysis of the indoor broadband power-line noise scenario," *IEEE Trans. Electromagn. Compat.*, vol. 52, no. 4, pp. 849–858, 2010.

[62] G. Prasad, H. Ma, M. Rahman, F. Aalamifar, and L. Lampe. A cumulative power line noise generator. [Online]. Available: http://www.ece.ubc.ca/~gauthamp/PLCnoise
[63] W. Chen and J. Choma, *Feedback Networks: Theory and Circuit Applications (Advanced Series in Circuits and Systems)*. World Scientific Press, 2007.
[64] C. R. Paul, *Analysis of multiconductor transmission lines*. John Wiley & Sons, 2008.

**Gautham Prasad** received the B. Eng degree in Electronics and Communications Engineering from PES Institute of Technology, Bangalore, India in 2012, and the M. S. degree in Electrical and Computer Engineering from the University of Florida, Gainesville, FL in 2014. He is currently working toward the Ph. D. degree with the Department of Electrical and Computer Engineering at The University of British Columbia, Vancouver, BC.

**Lutz Lampe** (M'02, SM'08) received the Dipl.-Ing. and Dr.-Ing. degrees in electrical engineering from the University of Erlangen, Germany, in 1998 and 2002, respectively. Since 2003, he has been with the Department of Electrical and Computer Engineering, The University of British Columbia, Vancouver, BC, Canada, where he is a Full Professor. His research interests are broadly in theory and application of wireless, power line, optical wireless and optical fibre communications. Dr. Lampe was the General (Co-)Chair for 2005 International Conference on Power Line Communications and Its Applications (ISPLC), 2009 IEEE International Conference on Ultra-Wideband (ICUWB) and 2013 IEEE International Conference on Smart Grid Communications (SmartGridComm). He is currently an Associate Editor of the IEEE WIRELESS COMMUNICATIONS LETTERS and the IEEE COMMUNICATIONS SURVEYS AND TUTORIALS and has served as an Associate Editor and a Guest Editor of several IEEE transactions and journals. He was a (co-)recipient of a number of best paper awards, including awards at the 2006 IEEE ICUWB, the 2010 IEEE International Communications Conference (ICC), and the 2011 IEEE ISPLC. He is co-edior of the book Power Line Communications: Principles, Standards and Applications from Multimedia to Smart Grid, published by John Wiley & Sons in its 2nd edition in 2016.

**Sudip Shekhar** (S00M10SM14) received the B.Tech. degree (Hons.) in electrical and computer engineering from the Indian Institute of Technology, Kharagpur, in 2003 and the M.S. and Ph.D. degree in electrical engineering from the University of Washington, Seattle in 2005 and 2008, respectively. From 2008 to 2013, he was with Circuits Research Lab, Intel Corporation, Hillsboro, OR, where he worked on high-speed I/O architectures. He is currently an Assistant Professor of electrical and computer engineering at the University of British Columbia. His research interests include circuits for high-speed electrical and optical I/O interfaces, frequency synthesizers, and wireless transceivers. Dr. Shekhar was a recipient of the IEEE TRANSACTIONS ON CIRCUITS AND SYSTEMS Darlington Best Paper Award in 2010 and a corecipient of IEEE Radio-Frequency IC Symposium Best Student Paper Award in 2015.